

AD-A171 670

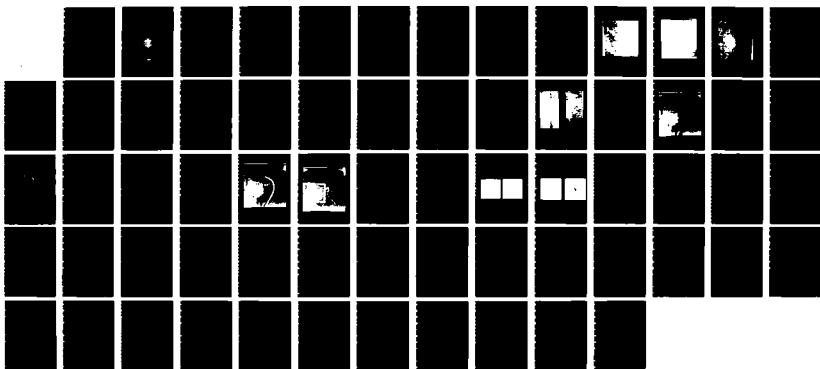
ANALYSIS OF SURFACE PATTERNS OVER COBB SEAMOUNT USING  
SYNTHETIC-APERTURE RADA IMAGERY(U) NAVAL ACADEMY  
ANNAPOLIS MD C B FREISE 27 MAY 86 USNA-TSPR-136

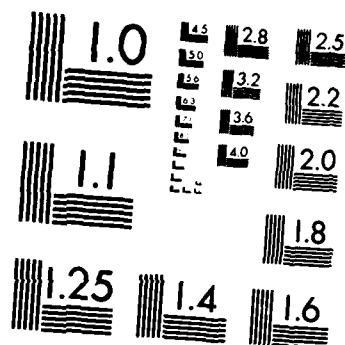
1/1

UNCLASSIFIED

F/G 17/9

NL





MICROCOPY RESOLUTION TEST  
 NATIONAL BUREAU OF STANDARDS-1963-A

15

# A TRIDENT SCHOLAR PROJECT REPORT

NO.  
136

ANALYSIS OF SURFACE PATTERNS OVER COBB SEAMOUNT  
USING SYNTHETIC-APERTURE RADAR IMAGERY



DTIC  
ELECTE  
SEP 8 1986  
S B

UNITED STATES NAVAL ACADEMY  
ANNAPOLIS, MARYLAND  
**1986**

This document has been approved for public  
release and sale; its distribution is unlimited.

AD-A171 670

DTIC FILE COPY

UNCLASSIFIED

SECURITY CLASSIFICATION OF THIS PAGE (When Data Entered)

REPORT DOCUMENTATION PAGE		READ INSTRUCTIONS BEFORE COMPLETING FORM
1. REPORT NUMBER	2. GOVT ACCESSION NO.	3. RECIPIENT'S CATALOG NUMBER
U.S.N.A. - TSPR; no. 136 (1986)	AD-A171 670	
4. TITLE (and Subtitle)		5. TYPE OF REPORT & PERIOD COVERED
ANALYSIS OF SURFACE PATTERNS OVER COBB SEAMOUNT USING SYNTHETIC-APERTURE RADAR IMAGERY		Final: 1985/1986
7. AUTHOR(s)		6. PERFORMING ORG. REPORT NUMBER
Freise, Clark Bruce		
9. PERFORMING ORGANIZATION NAME AND ADDRESS		8. CONTRACT OR GRANT NUMBER(s)
United States Naval Academy, Annapolis.		
11. CONTROLLING OFFICE NAME AND ADDRESS		10. PROGRAM ELEMENT, PROJECT, TASK AREA & WORK UNIT NUMBERS
United States Naval Academy, Annapolis.		
14. MONITORING AGENCY NAME & ADDRESS (if different from Controlling Office)		12. REPORT DATE
		27 May 1986
		13. NUMBER OF PAGES
		60
		15. SECURITY CLASS. (of this report)
		15a. DECLASSIFICATION/DOWNGRADING SCHEDULE
16. DISTRIBUTION STATEMENT (of this Report)		
This document has been approved for public release; its distribution is UNLIMITED.		
17. DISTRIBUTION STATEMENT (of the abstract entered in Block 20, if different from Report)		
This document has been approved for public release; its distribution is UNLIMITED.		
18. SUPPLEMENTARY NOTES		
Accepted by the U.S. Trident Scholar Committee.		
19. KEY WORDS (Continue on reverse side if necessary and identify by block number)		
Oceanography Seamounts Ocean waves Synthetic aperture radar Ocean currents		
20. ABSTRACT (Continue on reverse side if necessary and identify by block number)		
<p>Anomolies in surface wave patterns observed on SEASAT Synthetic-Aperture Radar (SAR) imagery over Cobb Seamount are examined. These anomalies are the surface expression of currents interacting with the seamount. The wavelengths of the imaged surface patterns are extracted with advanced SAR digital image processing techniques. Nine of the ten detected wavelengths match the expected spectral wavelength envelope of the internal waves that are calculated using</p> <p>(OVER)</p>		

DD FORM 1 JAN 73 1473

EDITION OF 1 NOV 68 IS OBSOLETE

S/N 0102-LF-014-6601

UNCLASSIFIED

SECURITY CLASSIFICATION OF THIS PAGE (When Data Entered)

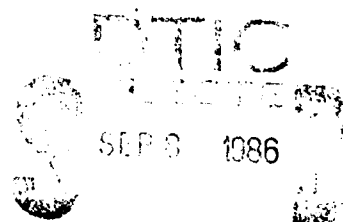
UNCLASSIFIED

SECURITY CLASSIFICATION OF THIS PAGE (When Data Entered)

oceanographic data. The results show that the wavelengths of the surface pattern imaged are actually the surface manifestation of internal waves on a subsurface density interface. The internal waves are created by current flow over and around Cobb Seamount disturbing the density interface.



✓



B

A-1

S/N 0102- LF-014-6601

UNCLASSIFIED

SECURITY CLASSIFICATION OF THIS PAGE(When Data Entered)

U.S.N.A. - Trident Scholar project report; no. 136 (1986)

"Analysis of Surface Patterns Over Cobb Seamount Using  
Synthetic-Aperture Radar Imagery"


A Trident Scholar Project Report

by

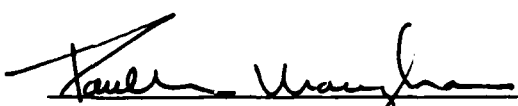
Midshipman Clark Bruce Freise, 1986

U. S. Naval Academy

Annapolis, Maryland

  
Professor Jerome Williams

Department of Oceanography

  
Visiting Prof. Paul Maughan

Department of Oceanography

Accepted for Trident Scholar Committee

  
Chairman

  
Date

ANALYSIS OF SURFACE PATTERNS OVER COBB SEAMOUNT USING  
SYNTHETIC-APERTURE RADAR IMAGERY

ABSTRACT

Anomalies in surface wave patterns observed on SEASAT Synthetic-Aperture Radar (SAR) imagery over Cobb Seamount are examined. These anomalies are the surface expression of currents interacting with the seamount. The wavelengths of the imaged surface patterns are extracted with advanced SAR digital image processing techniques. Nine of the ten detected wavelengths match the expected spectral wavelength envelope of the internal waves that are calculated using oceanographic data. The results show that the wavelengths of the surface pattern imaged are actually the surface manifestation of internal waves on a subsurface density interface. The internal waves are created by current flow over and around Cobb Seamount disturbing the density interface.

TABLE OF CONTENTS

Abstract .....	p. 1
Introduction .....	p. 4
History and Background .....	p. 8
Methods .....	p.12
Results .....	p.22
Conclusions .....	p.41
Appendix A .....	p.43
Acknowledgements .....	p.53
Bibliography .....	p.55



# LIST OF FIGURE AND TABLES

<u>Figures</u>	<u>Page</u>
1. Shallow water SAR imagery .....	5
2. Rockaway Seamount .....	6
3. Ormonde Seamount .....	7
4. Chart of Cobb Seamount area .....	14
5. Seasonal buoyancy frequency tables .....	16
6. Optical vs. digital SAR processing .....	18
7. Enhanced 466 image .....	20
8. Surface pattern model .....	23
9. Bow wave manifestations .....	28
10. Internal wave generation area .....	29
11. Test and reference areas .....	30
12. Reference area image and power spectrum .....	31
13. Test area image and power spectrum .....	32
14. Test area power spectrum model .....	33
15. Reference area full power spectrum .....	34
16. Test area full power spectrum .....	35
17. Reference area half power spectrum .....	36
18. Test area half power spectrum .....	37
19. Comparison of half power spectrums .....	38
A1. SAR sensor geometry .....	44
A2. Time difference .....	45
A3. Real vs. synthetic aperture size .....	47
A4. Doppler shift .....	50
A5. Doppler history .....	51

<u>Tables</u>	<u>Page</u>
1. Data summary .....	21
2. Significant wavelengths .....	40

## INTRODUCTION

Subsurface ocean currents flowing over underwater features have been shown, by Lee and Beardsley (1974) among others, to alter the surface wave pattern. The alteration of the surface wave pattern is caused by the underwater feature disrupting the current flow which translates by hydrodynamic processes to the surface of the ocean with consequential alteration of the surface waves. Satellite observations of the wave alterations using a synthetic-aperture radar sensor have been shown by Kasischke et. al.(1984) to have a high correlation to the underlying bathymetry (Fig. 1). Similar results have also been reported by other scientists in many shallow water areas with currents (Fu and Holt, 1982; McCandless and Mrazek, 1982).

The alteration of surface wave patterns in the vicinity of deep water features has been reported by Robinson (1985), but the literature does not report a direct correlation between imaged patterns and bathymetry as can be seen in the imagery of Rockaway and Ormonde Seamounts (Fig.2 & 3). Assuming that the same hydrodynamic dependence on subsurface currents that applies to shallow water imaging applies to deep water imaging, a research project was undertaken to

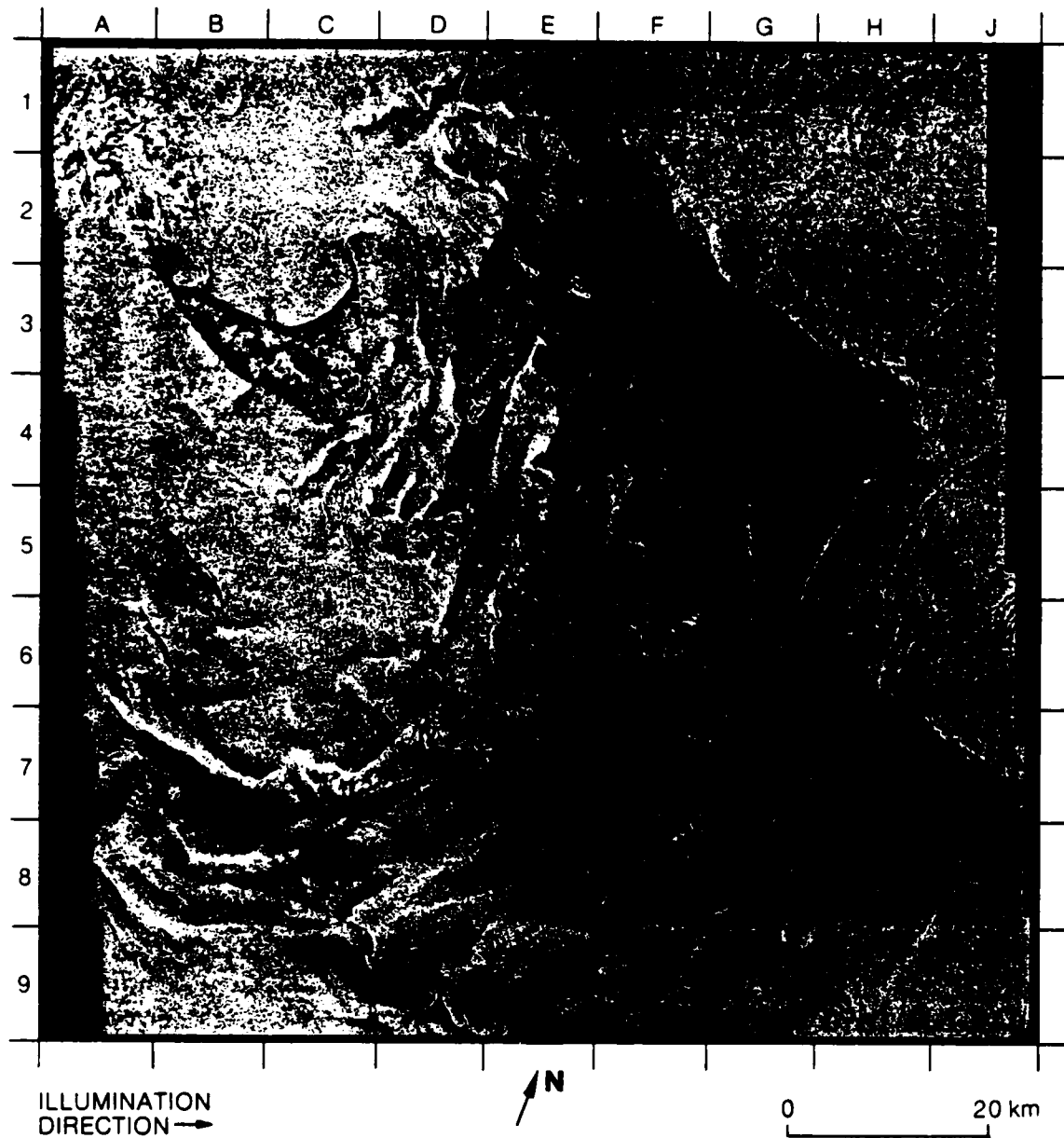


Figure 1

Shallow water imagery taken over Nantucket Shoals.

(Imagery taken from Fu and Holt, 1982)

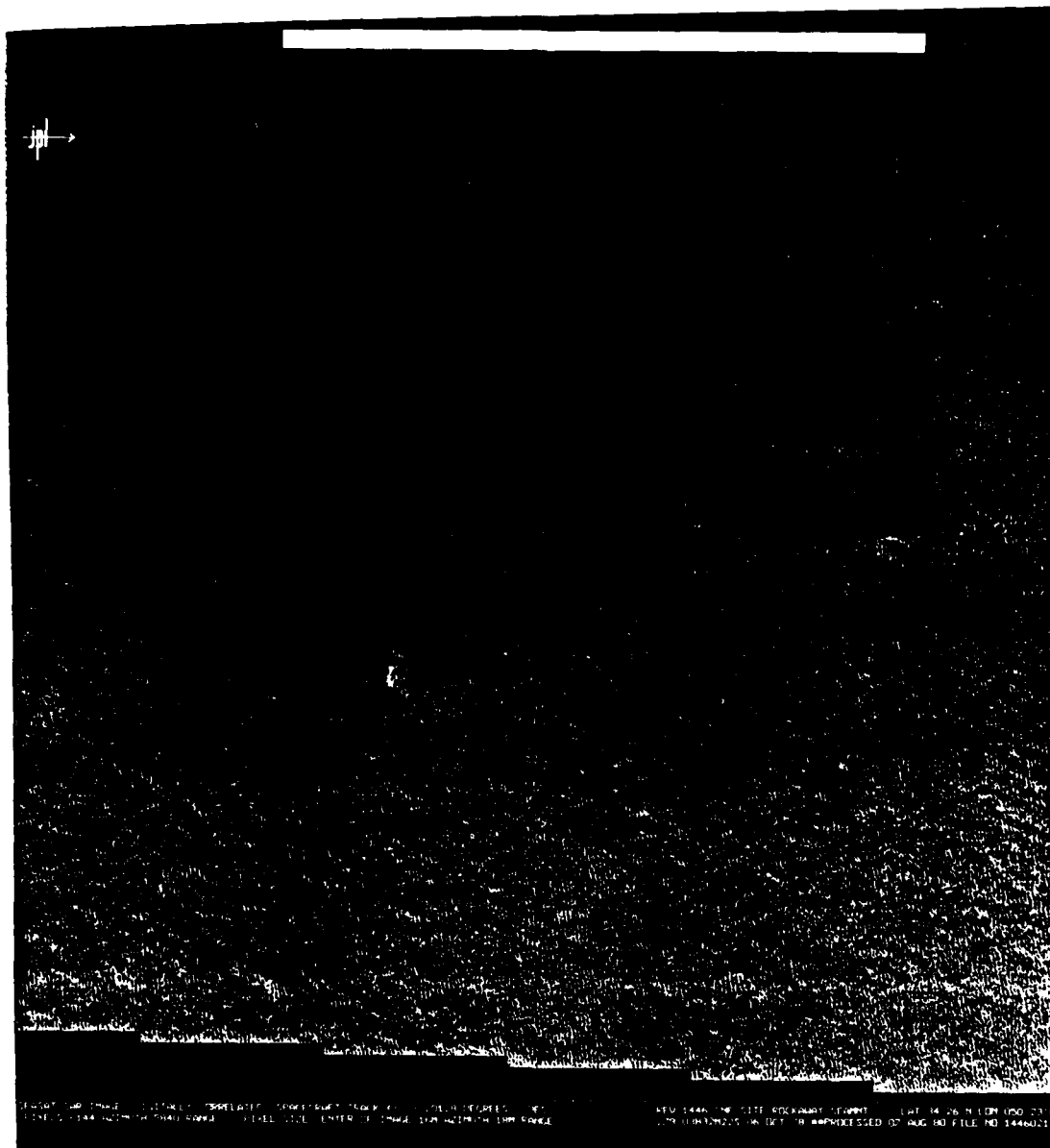


Figure 2

Rockaway Seamount (800 meter depth)

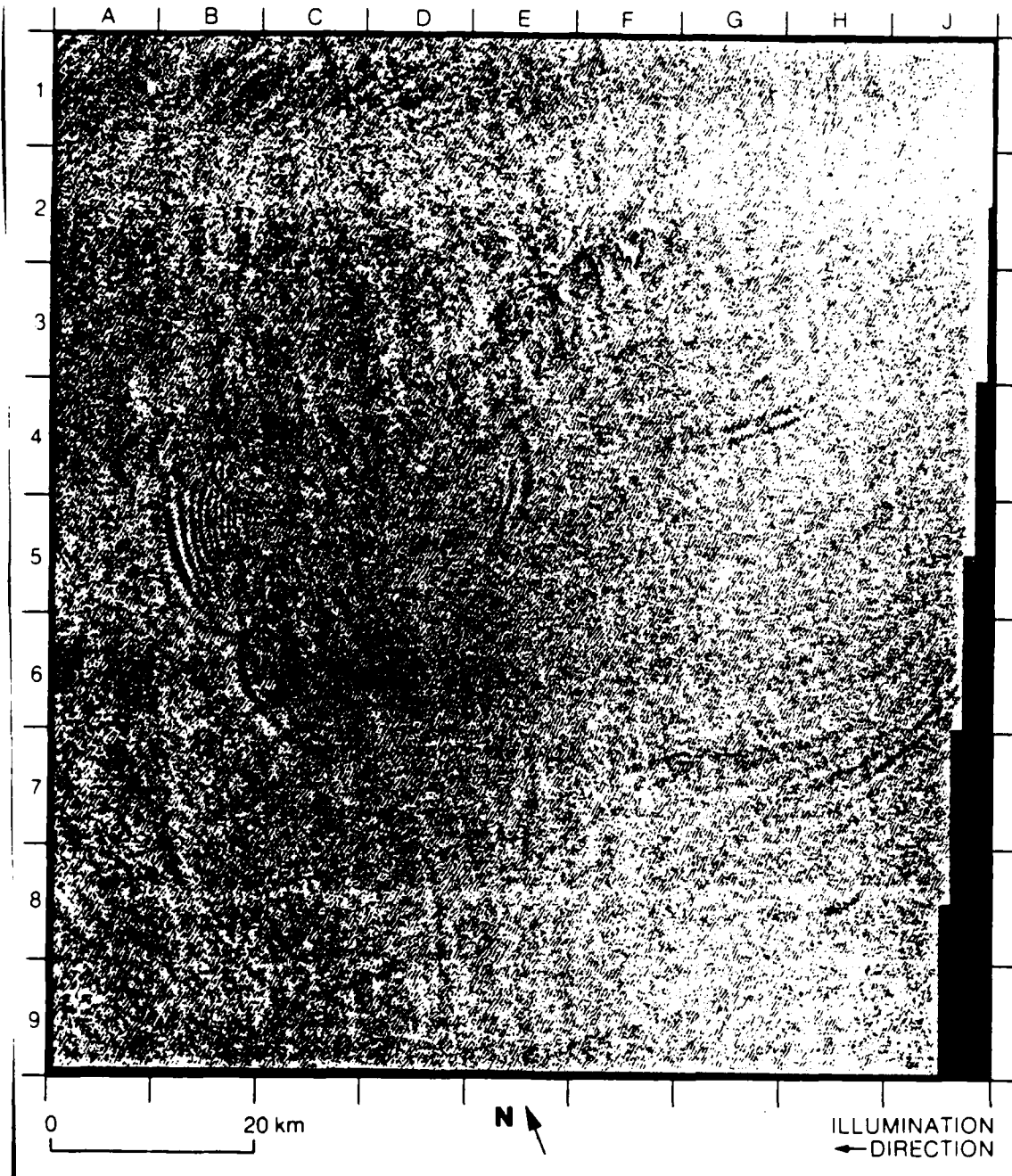


Figure 3

Ormonde Seamount (25 meter depth)

examine the surface patterns associated with current flow over Cobb Seamount and relate the surface patterns to specific hydrodynamic phenomena.

#### HISTORY AND BACKGROUND

Dr. Gifford Ewing, an oceanographer well known for his creative thinking, in the early 60's postulated the use of remote platforms in the detection and measurement of oceanographic conditions and data. Ewing (1965) noted that until this time the thought of

"oceanography from a satellite sound(ed) incongruous and, to a generation of scientists accustomed to Nansen bottles and reversing thermometers, absurd".

This was because most oceanographic observations until then were performed through the laborious process of using in-situ instruments and attempting to extrapolate from the local changes the larger scale phenomena creating the changes. However, with the introduction of remote sensors the possibility of observing synoptic scale phenomena was created.

The first remote sensors were visible wavelength sensors (such as cameras) used aboard aircraft. Visible wavelength sensors are useful in the detection of current fronts, wave heights, and wind directions

(Duntley, 1965). Visible wavelengths are very susceptible to attenuation in the atmosphere and remote sensing is possible only if the area to be imaged is naturally illuminated by the sun or moon at the time of imaging.

Infrared wavelength sensors (familiar to many from weather satellite imagery), are one of the most commonly used sensor types. Infrared (IR) wavelength sensors (1 - 10 micrometer wavelength) are used to measure relative differences in thermal activity on the Earth's surface and in the atmosphere. This allows the IR sensors to detect clouds, surface currents, warm water and cold water interfaces, and urbanized areas. Areas of colder water which usually contain higher biological activity can be located in this manner. IR sensors are also used in the development of daily weather forecasts due to the ability of IR sensors to image cloud formations and fronts. IR sensors are not dependant on direct illumination from the sun, as visible sensors are, since they measure the amount of thermal radiation emitted by the surface rather than reflected radiation. However, most IR wavelengths are highly attenuated by the atmosphere, particularly by clouds. This attenuation limits the capability of these sensors in imaging the oceans in areas where

storms, fog, or cloud cover are present.

A family of sensors that are least attenuated by the atmosphere are sensors using the microwave wavelength region (wavelengths of 0.1 to 100 cm.). The longer wavelengths used by the microwave sensors are only scattered by the very large rain drops present in major storm clouds. This allows these sensors to image through all but the densest clouds. The first space-borne microwave sensor was the radiometer on board the Mariner 2 that was used to measure surface temperature, atmospheric water vapor, ice cover, and sea temperature on Venus (Carver, Elachi, and Ulaby, 1985). One type of centimeter wavelength device is the active microwave sensor. Those sensors do not require outside illumination because the sensors send out energy and measure the reflected signal energy.

One active microwave sensor is the synthetic-aperture radar (SAR). SAR is an imaging radar that creates a very high resolution (typically 10-20 m.) image through the data collection and processing technique known as aperture synthesis (Appendix A).

Carl Wiley first theorized aperture synthesis as an imaging method in 1951 while working for Goodyear. In 1961 the first synthetic-aperture radar sensor was used by L.J. Cutrona to image ground features



(Harger, 1970). A space-borne SAR sensor was first used to image the oceans in 1978 when the SEASAT satellite was launched. Though the satellite failed after 110 days, 100 million square kilometers of SAR data were obtained (Pravdo et.al., 1983).

Included in the SEASAT data are the imagery containing surface manifestations of the underlying bathymetry. The information drawn from the imagery has stimulated researchers to attempt to model the return signal created by current flow over shallow water bars and shoals (Alpers and Henning, 1985). The models work well for the sensor and area data from which they were derived, but none has proven successful for all radar wavelengths and conditions.

SAR imagery in areas with deep water topographic features also shows surface patterns associated with the disruption of currents. However, since the features creating the disruption are deeper than shoals or sand bars the imagery does not show patterns conforming to the underlying bathymetry.

A commonly imaged surface pattern imaged in the region of deeper water features is an internal wave field (Robinson, 1985). For example, internal waves are often created by current flow over seamounts. Internal waves are large amplitude waves created by the disturbance of a stable density difference

interface. Such a disturbance could be caused by current flow over a seamount. Ewing showed that internal waves can manifest themselves in the surface wave pattern (Fu and Holt, 1982). These manifestations of internal waves in the surface wave pattern have been imaged by the SEASAT SAR sensor (Robinson, 1985).

#### METHODS

The ideal area for studying the surface manifestations of the subsurface current-seamount interaction with SAR imagery would be a deep flat ocean plain with one seamount peak reaching near the surface. The currents should be steady with a current meter situated on the seamount. The density structure of the water column above the seamount should include a strong thermocline (abrupt change in the temperature of the water column with depth) to enhance the potential for internal waves. The surface conditions should include a stable base wave pattern, in other words, the area should not be a wave generation area since the surface pattern would contain too many longer wavelength surface waves with no prevalent direction of propagation for analysis. This means that the ideal wind conditions would be lower, with

the winds only strong enough to develop the necessary capillary waves. Capillary waves are short wavelength waves (less than 2 cm.). Capillary waves are critical for SAR imaging because they are the waves that backscatter the transmitted pulse back to the sensor to create the image. Of course, the presence of multiple SAR images of the region is also important. Since not all SAR data shows the high degree of detail that would be preferable for analysis, it is best to find an area that has as many passes with strong details visible as possible.

Cobb Seamount was chosen for this project since it most closely matches the ideal conditions set forth. The seamount peak protrudes from the edge of the Cascadia Abyssal Plain off the Oregon coast to within 30 meters of the surface. There are no seamounts in the direct path of the North Pacific Drift before the current interacts with Cobb (Fig 4). The seamount is located in the North Pacific Drift which provides a steady  $1/3$  Knot of current in the month of July (Maughan, 1963). The tidal currents have not been directly measured, but the tidal height which is the actual wave created by the tidal forces has been measured on Cobb. By assuming a zero time delay between the tidal height and the tidal current (reasonable in the open ocean), an estimate of the

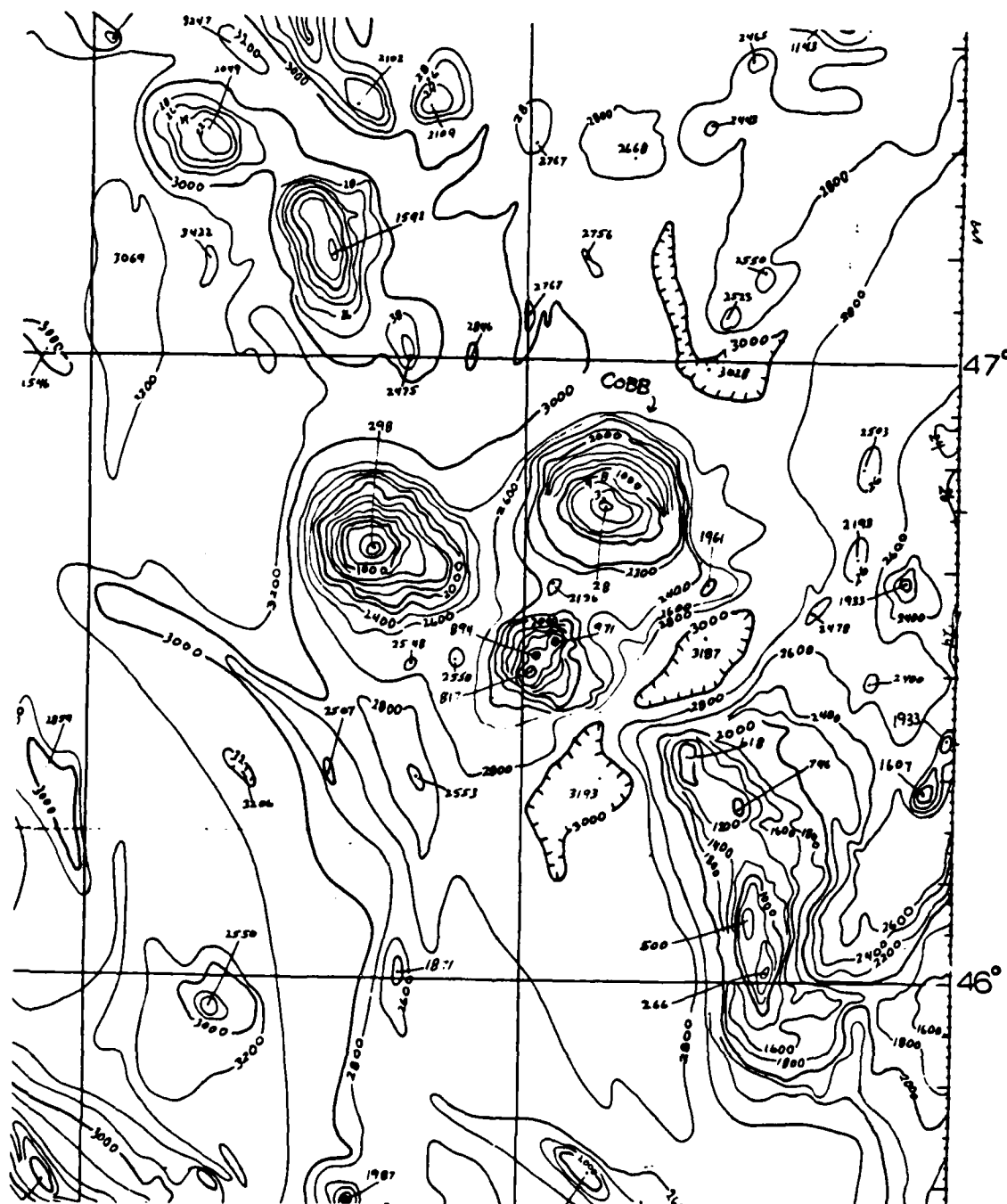


Figure 4

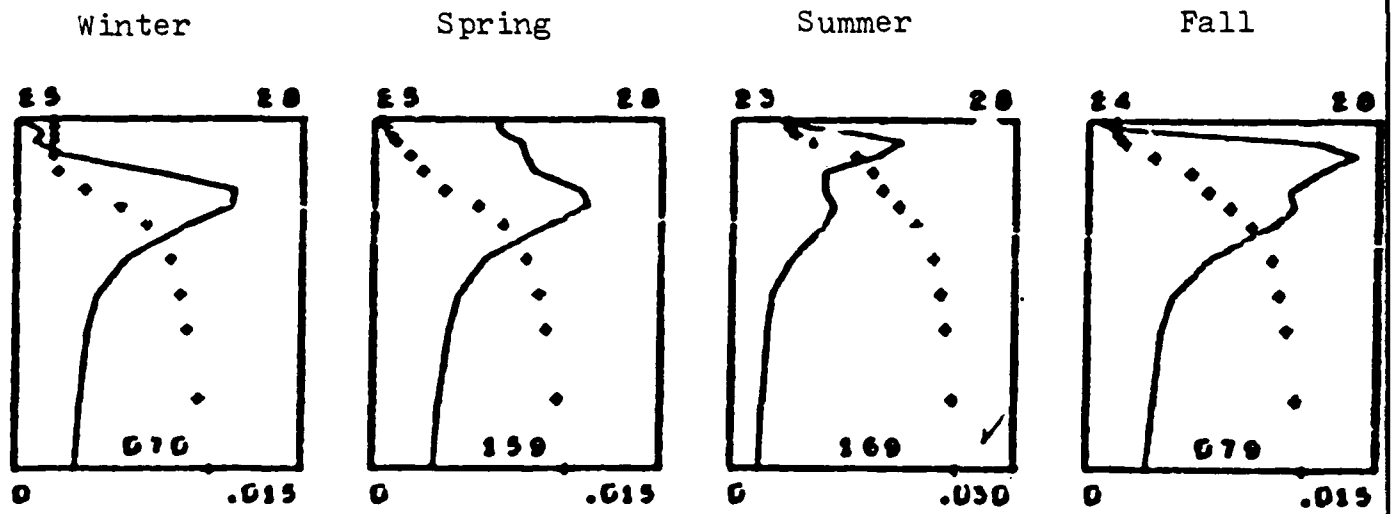
Chart of Cobb Seamount Region

(Cobb Seamount - 46 45.8'N., 130 48.6'W.)

tidal contribution to the current can be found. This is estimated to be up to one knot vectorially added to the steady N. Pacific Drift current (Apel, 1986).

The density distribution over the seamount was not directly available for Cobb at the time of SAR imaging, but temperature readings were available from Fleet Numerical Oceanography Center (FNOC), Monterey, California. This data shows a drop of 7.5 degrees celsius between 21 and 49 meters in depth, where the peak of the seamount is located. The data was compared to seasonal buoyancy frequency tables compiled by Bell, Mays, and DeWitt (1974). The buoyancy frequency tables (Fig. 5) show the Brunt-Vaisala frequency distribution by month and by region. The Brunt-Vaisala frequency is the natural harmonic frequency which internal waves and other density instability waves resonate. The temperature data showed similar changes in the water density by depth as the seasonal data. The temperature data available only contained readings at large steps (over 10 meters), and only to limited depths (less than 100 meters), so the seasonal data were used in the calculations.

The SAR data used for this study was from the SAR sensor on board the SEASAT satellite launched in 1978. Using a geo-location program from



Magnified Summer Curve

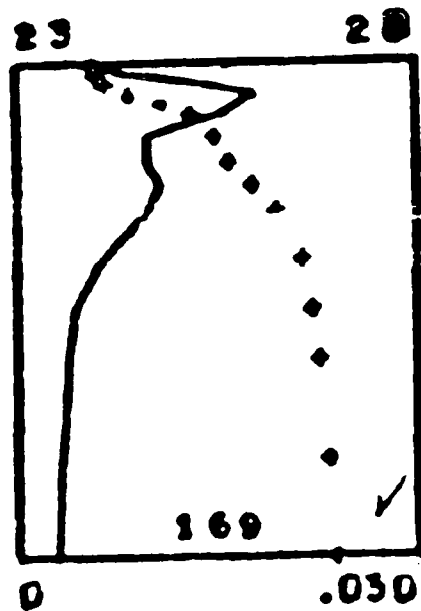


Figure 5

Seasonal buoyancy frequency tables.

(From Bell, Mays, and DeWitt, 1974)

Jet Propulsion Laboratory (JPL), it was determined that only three recorded SAR passes included data taken over Cobb Seamount. The three data sets were included in satellite revolutions 222, 466, 710. The data were originally transmitted from the satellite to the Goldstone, California ground station where the data were recorded.

From the recorded computer tapes of this data optical and digital image processing can be performed (Fig. 6). The data from all passes is available on optical film for the SEASAT SAR. From inspection of the three revolutions it was decided that revolution 222 contained too little detail for the image to be of use in the analysis. The data from over Cobb contained in revolutions 466 and 710 appeared on the optical film to contain sufficient detail for analysis. The data from 466 and 710 were processed digitally and prepared for analysis.

Digital processing involves taking the original transmitted data and completing the entire coherent addition process for the return pulses that contain data from over Cobb Seamount. The output image is then a digital image with each resolution element having its own identity and intensity. A linear enhancement was also performed to improve contrast within the image. The digital processing was



Optical



Digital

Figure 6

Optically and digitally processed imagery of SAR data.

(Imagery from Fu and Holt, 1982)



performed on the SAR digital processing system at JPL, with the enhancements being performed at Naval Research Laboratory / Digital Image Processing Laboratory (NRL/DIPL), Washington, D.C..

The surface conditions present when the Rev. 466 data were taken was favorable for SAR imaging. The winds at the time of imaging were light according to data from FNOC. A well developed wave pattern was already present in the area. For the 710 data, however, the winds were 18 knots. This could have caused some of the detail in the surface pattern to have been obscured. Because of this obscuration, it was decided to drop 710 from further analysis and focus on the imagery from the 466 data (Fig. 7)

To analyze the interaction of the current with the seamount and the surface manifestation of the interaction, accurate bathymetric data was obtained. Accurate bathymetry for Cobb Seamount was available from the Naval Oceanographic Command, Bay St. Louis, Mississippi. This data allowed the determination of exact location of the seamount and aided in modeling the interaction.

A summary of the data collected for this project is contained in Table 1.

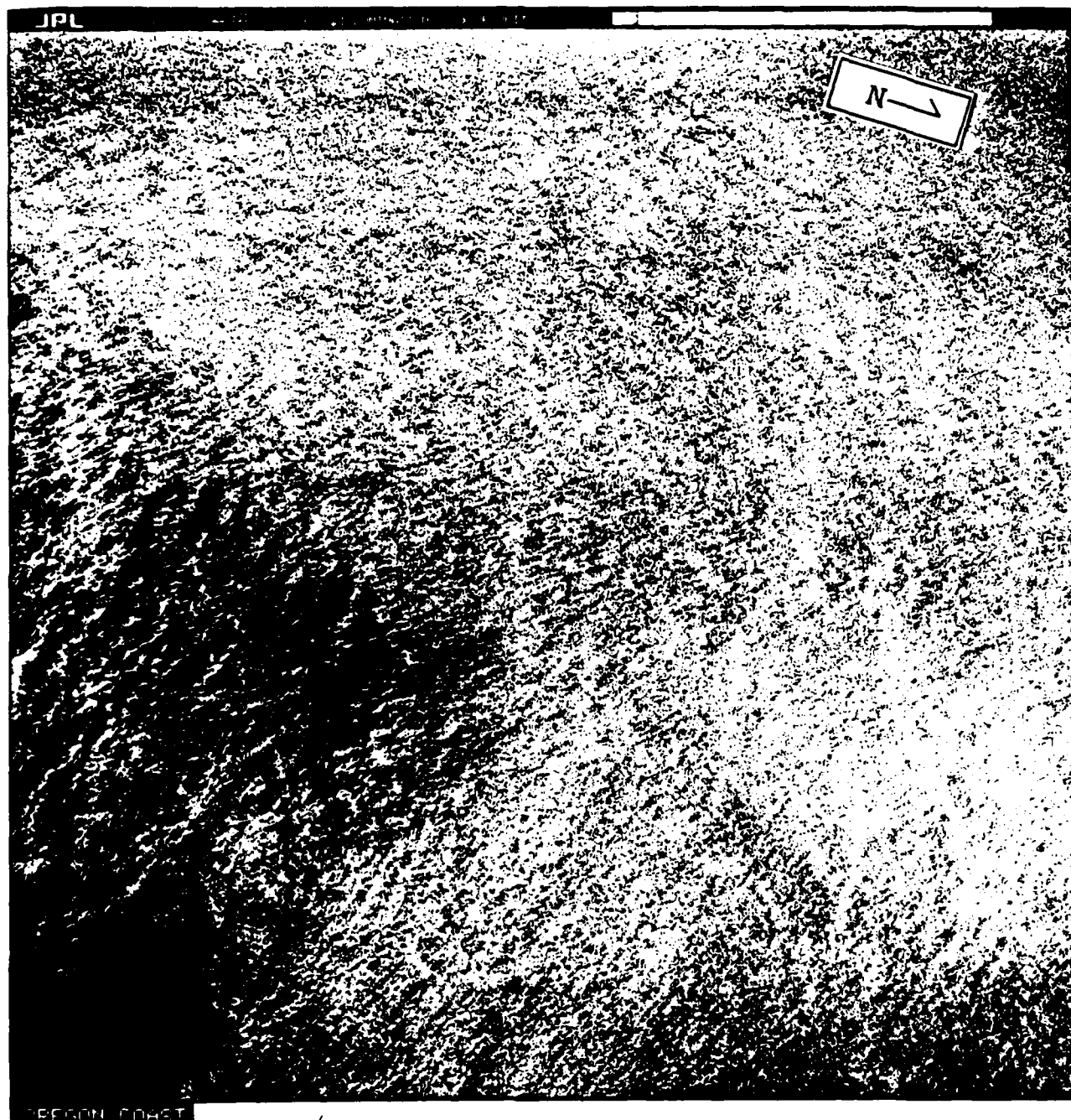


Figure 7

Enhanced image of 466 data over Cobb Seamount.

# DATA SUMMARY

DATA:	VALUE/FORM:	SOURCE OR DERIVED FROM:
Bathymetry	Charts	Cobb, Rockaway, and Ormonde Seamount charts obtained from Naval Oceanographic Office, Bay St. Louis, MS.
Steady Current	1/3 Knot	Maughan, 1963.
Tidal Current	2/3 Knot	From an estimated maximum current of 1 knot. The tidal height is two hours from max. height (Schwinderski, 1981). The estimate was developed with the aid of Dr. Apel (APL).
Temperature Distribution	XBT Data	From Fleet Numerical Oceanographic Center, Monterey, CA.
Brunt-Vaisala	N	From Bell, Mays, and DeWitt, 1974.
466 SAR Data		Original data from Jet Propulsion Laboratory, Pasadena, CA. Data enhanced by NRL/DIPL, Washington, D.C..
Power Spectrum		NRL/DIPL, Washington, D.C..

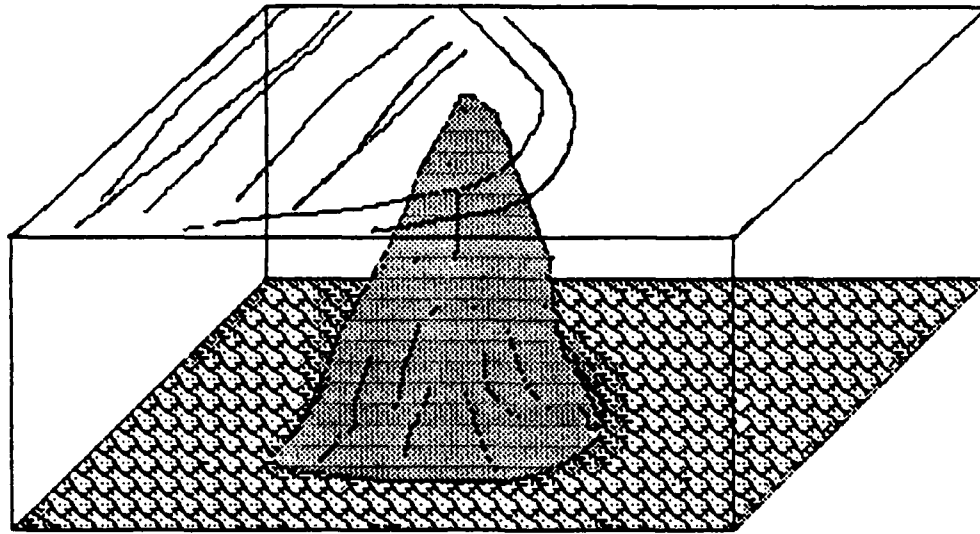
Table 1

Summary of collected data.

### RESULTS

From examining imagery of Rockaway and Ormonde Seamounts (Fig. 2 & 3), a qualitative model was developed for comparison to SAR imagery taken over Cobb Seamount. The model was developed to aid in the understanding of the dynamics involved in the interaction between the current and the seamount, and the manifestation of the interaction in the surface wave pattern. The model assumes a homogeneous background wave pattern onto which the manifestation will be imprinted. The manifestation is expected to have two major constituents: bow waves and internal waves (Fig. 8).

Bow waves are a semiparabolic wave pattern created by the slowing of a current front by an obscuring feature, and the flow of the current around the created lower velocity area. The waves form, in the case of a point stoppage of the current as would be created by a seamount, as semiparabolic waves pointing into the current and cupping around the feature. Since Cobb reaches to within 30 meters of the surface, a well developed bow wave pattern would be expected to form. Such waves should be visible in the SAR imagery since the change in current velocity and the associated current shear will affect the surface wave pattern. The pattern, however, can best



SURFACE PATTERN MODEL - SIDE VIEW

SURFACE PATTERN MODEL - TOP VIEW

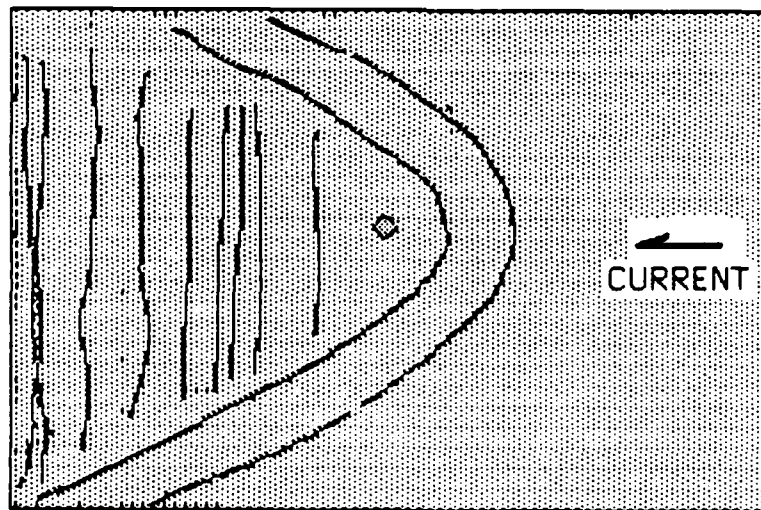


Figure 8

Surface pattern model.

(Bow wave and internal wave manifestations)

be analyzed through qualitative analysis since the bow waves do not have a constant wavelength or common direction of propagation. The bow waves will not propagate, as surface waves would, since they are only the manifestation of a current shear. If the waves did have a constant wavelength and common direction of propagation, they could be quantitatively described by using an analytical methodology. A commonly used methodology is to develop a power spectrum of the surface wave pattern. A power spectrum is a transform of the digital information into a spectrum of energy returned versus direction of propagation and wavelength of the surface patterns imaged.

The possibility of internal waves is present in the area of Cobb. Internal waves are created when a strong density discontinuity (such as a strong thermocline) exists and the interface of the discontinuity is disturbed. A strong thermocline is present in the area of Cobb Seamount and the current flowing over Cobb would disturb the interface. Robinson (1985) has stated that internal waves have often been imaged by SAR sensors in the vicinity of seamounts. In the imagery taken of Rockaway Seamount, with the seamount peak located 800 meters below the ocean surface, internal waves are in evidence (Fig. 2). Internal waves are also in evidence in the

imagery of Oromonde Seamount (25 meter depth) (Fig. 3). Although Cobb is not as shallow as Ormonde or in the very strong flow of the Gulf Stream like Rockaway, it was predicted that internal waves would be imaged over Cobb also.

Current interaction with the normal development of internal waves, however, affects the internal wave wavelengths that will manifest themselves in the surface wave pattern. Internal waves created with minimal current flow or by simple displacement form with wavelengths determined by the natural buoyancy frequency (Brunt-Vaisala) determined by the density changes present. If a strong current is present, the internal waves are forced to oscillate at higher frequencies. This forcing causes the internal waves to form in an envelope of frequencies in the lee of the seamount. The envelope has a lower wavelength cutoff determined by:

$$\text{Wavelength} = \frac{C}{N} \quad \text{Eq. 1}$$

where C is the magnitude of the current  
N is the effective Brunt-Vaisala frequency  
(Apel, 1986).

The other end of the wavelength envelope is the determined from the Brunt-Vaisala frequency alone. The internal waves in this envelope will form in the lee of the seamount, then when the current abates the waves will travel over the seamount and

propagate out into the ocean in the direction opposite the original creating current (Apel, 1986). Using seasonal data for  $N$  in Eq.1 and a current estimate of 1/3 knot steady current and 2/3 knot tidal current adding, the lower end cutoff wavelength is 0.5 km. The imagery is therefore expected to contain manifestations of internal waves of variable wavelengths with all the wavelengths greater than one half a kilometer.

The combination of a bow wave pattern and the surface manifestation of the internal wave generation area is taken as the qualitative model of the expected imagery. A possible version of the model is shown by figure 8.

The revolution 466 digital imagery does show some similarities to the proposed model. There is a subtle signature from two bow waves (Fig. 9), although not nearly as clearly defined a signature as was expected. There is also an area that shows the presence of longer wavelength manifestations inside the bow waves. The pattern is confused as would be expected from the combination of multiple wavelength waves in one region (Fig. 10).

Performing a power spectrum analysis on the multiple wavelength waves is a proven method of quantifying the patterns imaged. The power spectrum



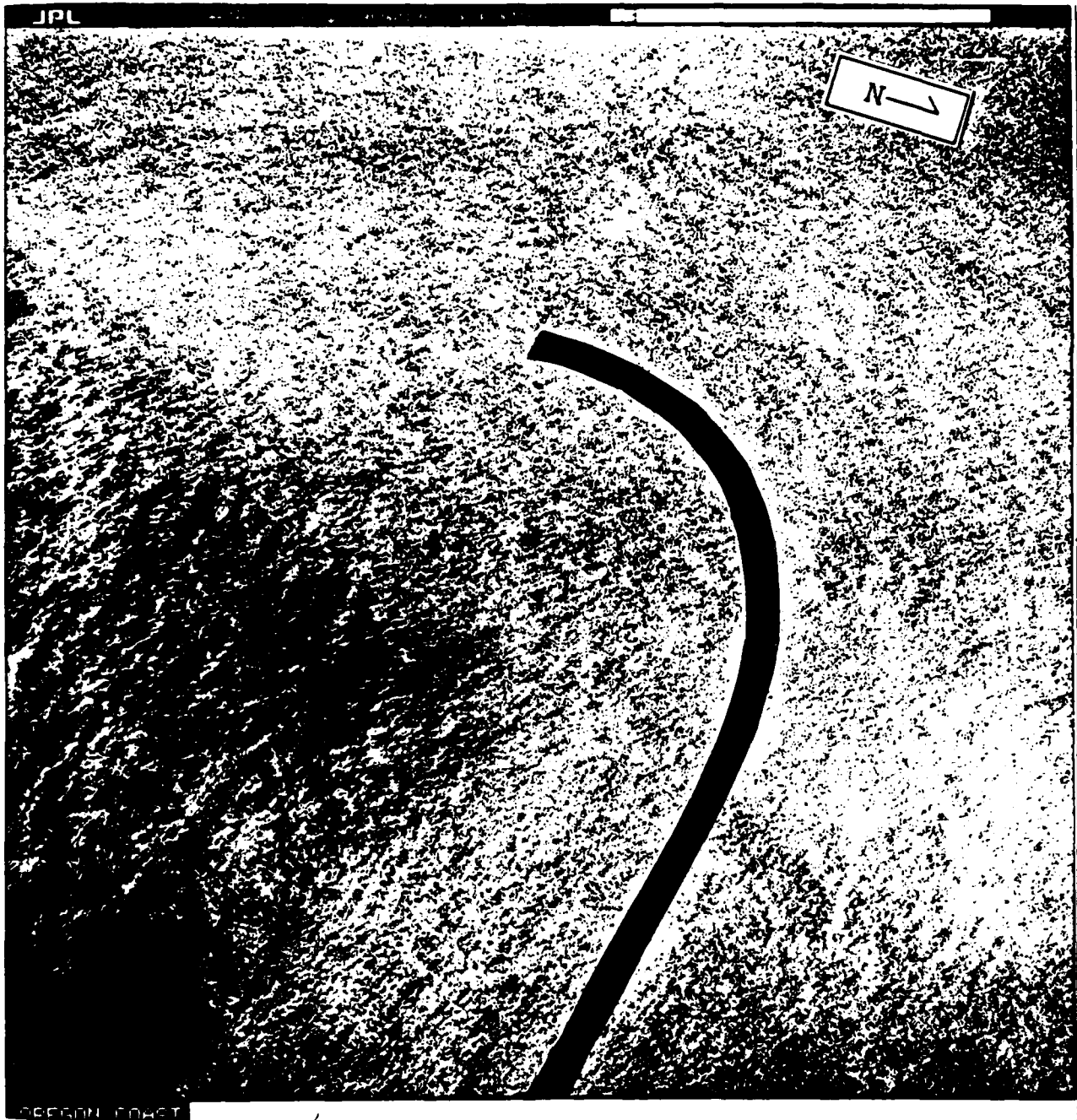


Figure 9

Bow wave manifestations on 466 enhanced imagery.

(Dark line is drawn between the two manifestations  
visible in image)

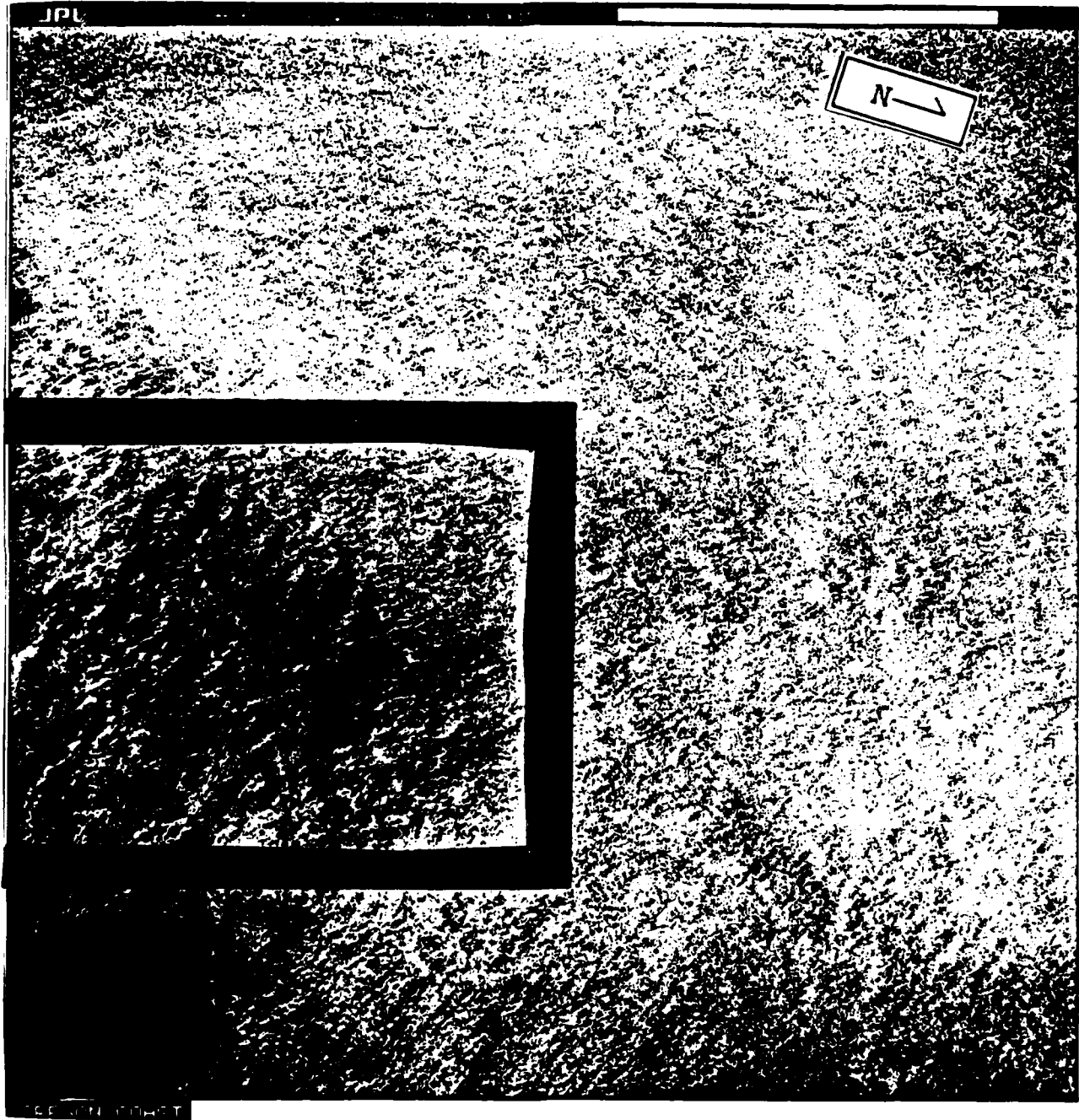


Figure 10

Possible internal wave generation region.

most commonly used is a representation of the returned power versus the wavelength and direction of propagation of the waves returning the power. The power spectrum used for this analysis were generated through the use of a Fast Fourier Transform contained in the software in the mainframe computers at Naval Research Laboratory (NRL/DIPL).

A power spectrum was developed of two areas in the 466 image (Fig. 11): a reference area that contains no manifestations of the current-seamount interaction, and a test area that is centered in the manifestations of the interaction (Fig. 12 & 13). From the power spectrum it was determined that the predominate direction of wave propagation was to or from the North-Northeast. Using this orientation, a directional slice was taken through the power spectrum (Fig. 14) to determine a two dimensional power spectrum (power vs. wavelength) (Fig. 15 & 16). These represent both the positive and negative directions of propagation possible in the image (180 degrees opposite). Since there should be perfect symmetry about the spectrum centerpoint for waves, one half of the spectrum showing only the positive direction wavelengths can be plotted, and expanded (Fig. 17 & 18). These can then be combined for easy comparison (Fig. 19).

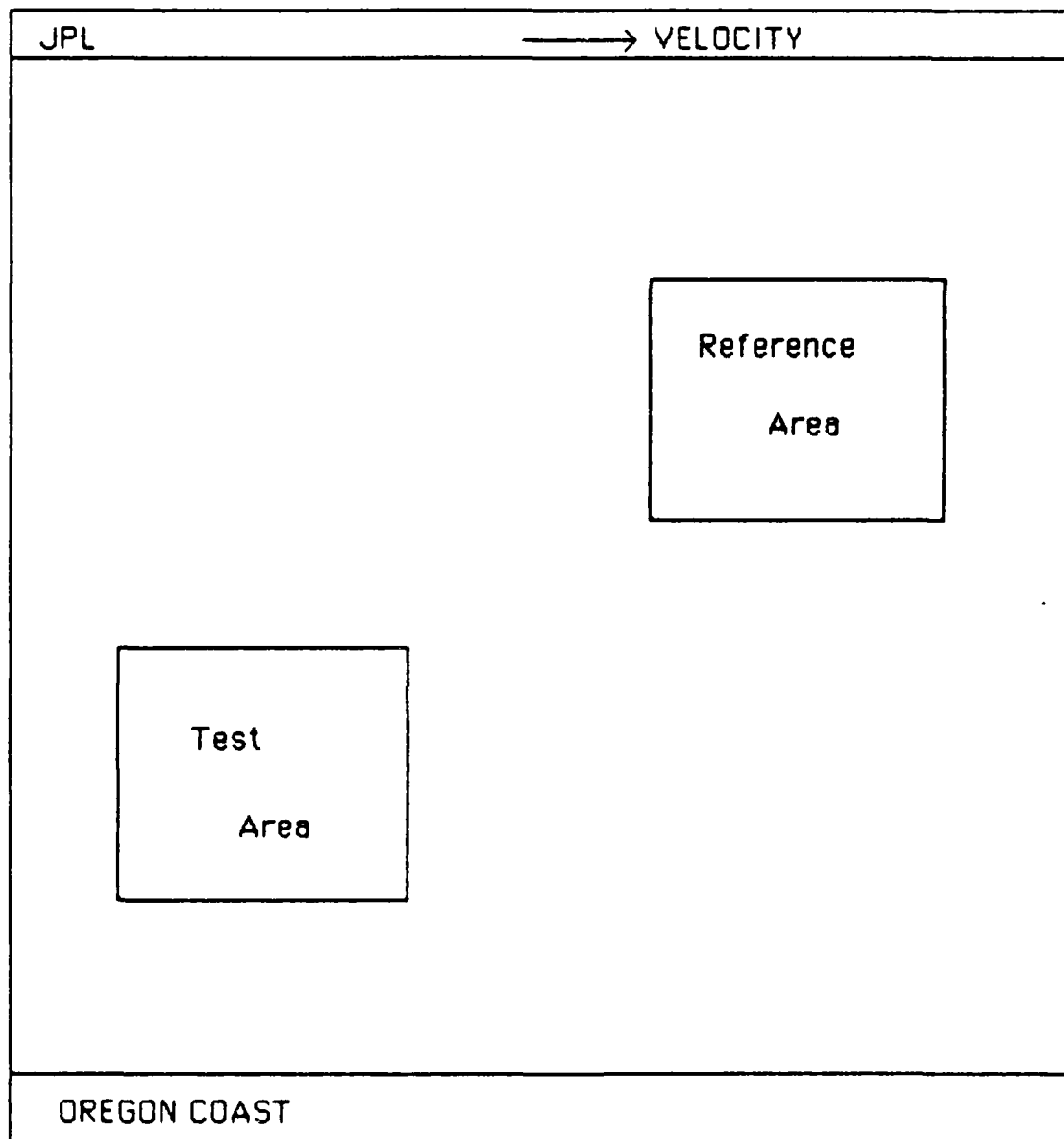


Figure 11

Areas used for power spectrums.

Test Area - contains manifestations of internal waves

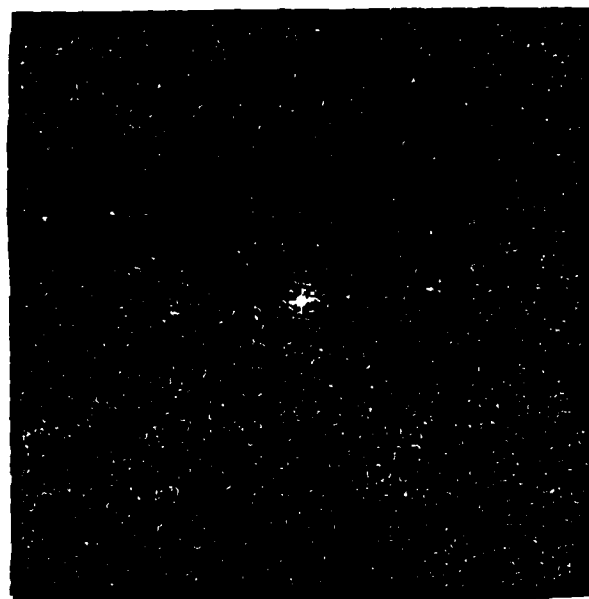
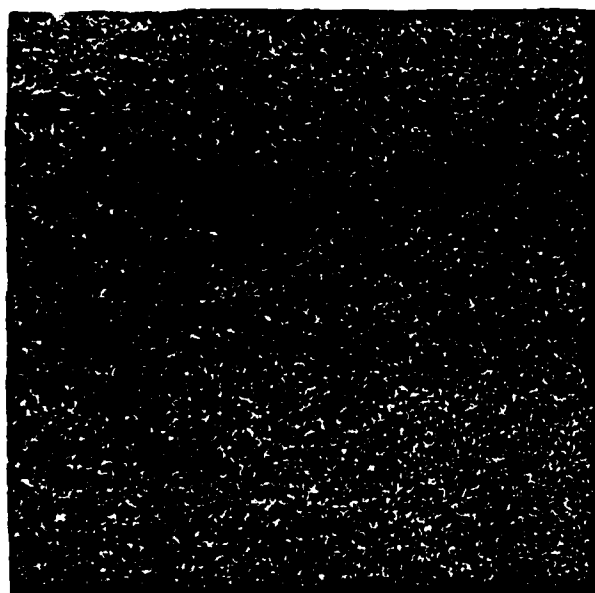
Reference Area - contains no manifestations

REFERENCE AREA OF COBB SEAMOUNT  
SEASAT SAR REV 466 IMAGE

2D IMAGE

2D POWER SPECTRUM

36.9 km Range



32.8 km Azimuth

Figure 12

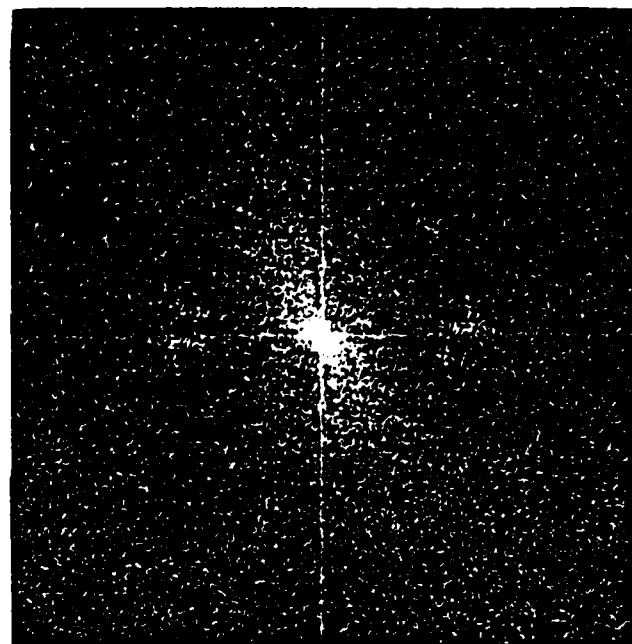
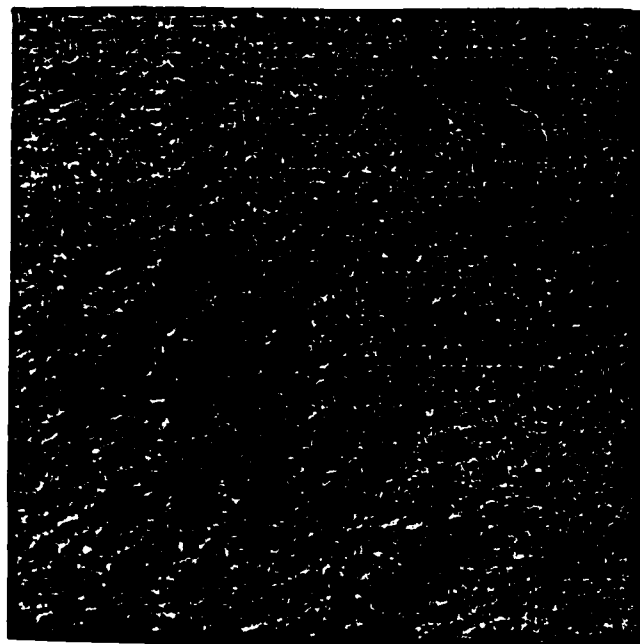
Image reference area and developed power spectrum.

COBB SEAMOUNT AREA  
SEASAT SAR REV 466 IMAGE

2D IMAGE

2D POWER SPECTRUM

36.9 km Range



32.8 km Azimuth

Figure 13

Image test area and developed power spectrum.

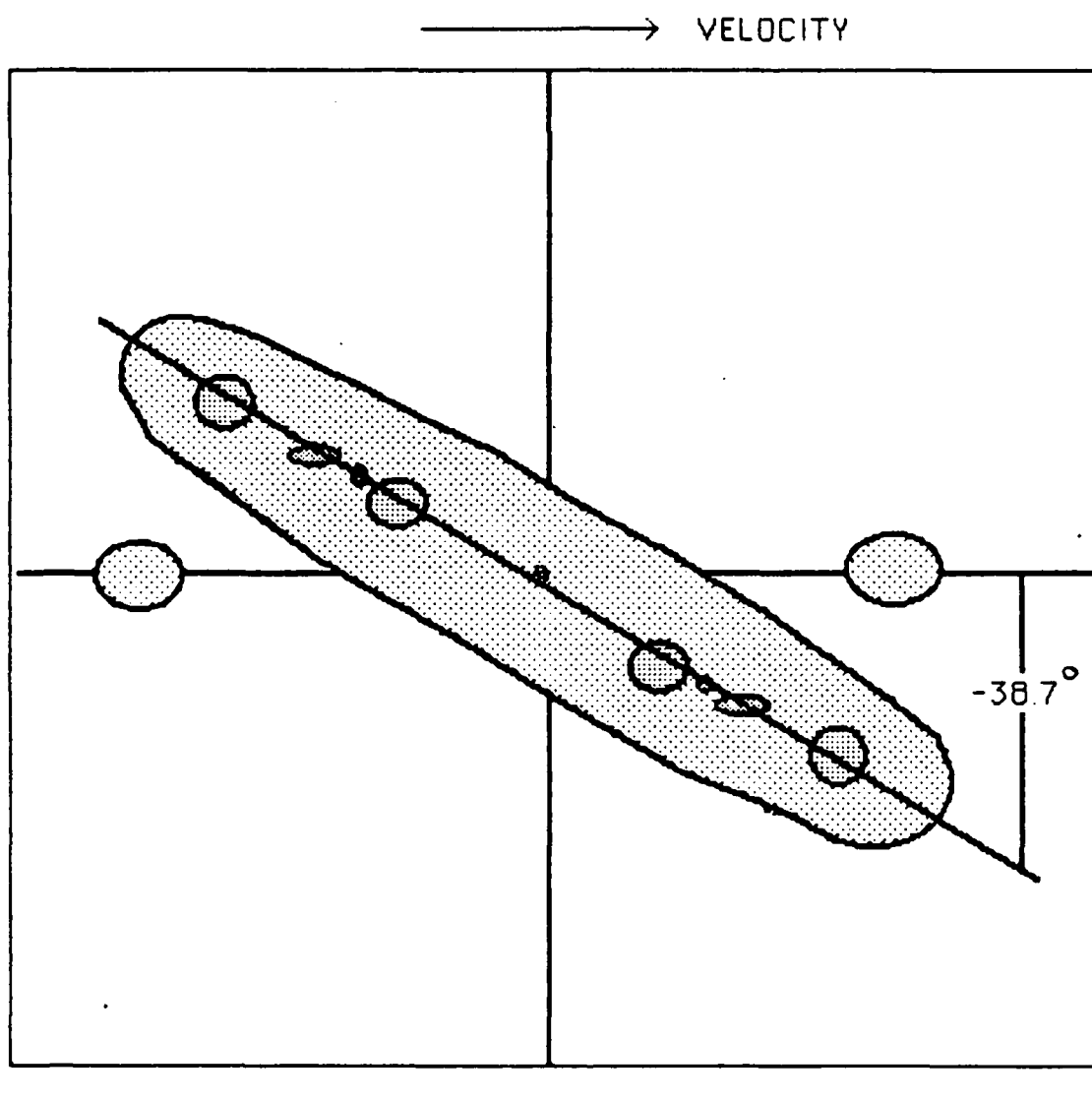


Figure 14

Model power spectrum of Cobb test area.

Darker areas represent wavelengths and directions of  
higher energy return.

POWER SPECTRUM-REFERENCE AREA FOR COBB SEAMOUNT  
SEASAT SAR REV 466 IMAGE

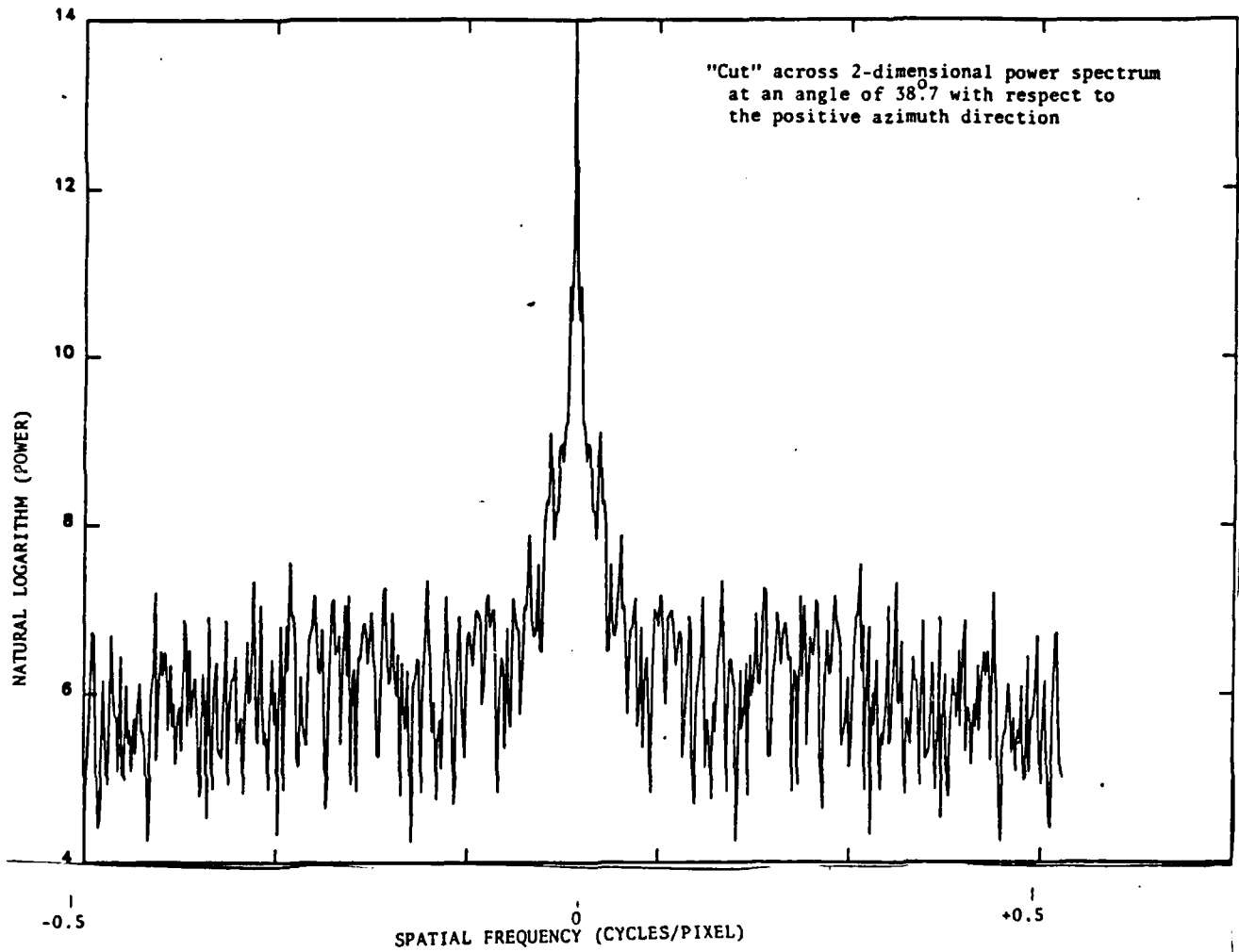


Figure 15

Full power spectrum of reference area.



POWER SPECTRUM-COBB SEAMOUNT AREA  
SEASAT SAR REV 466 IMAGE

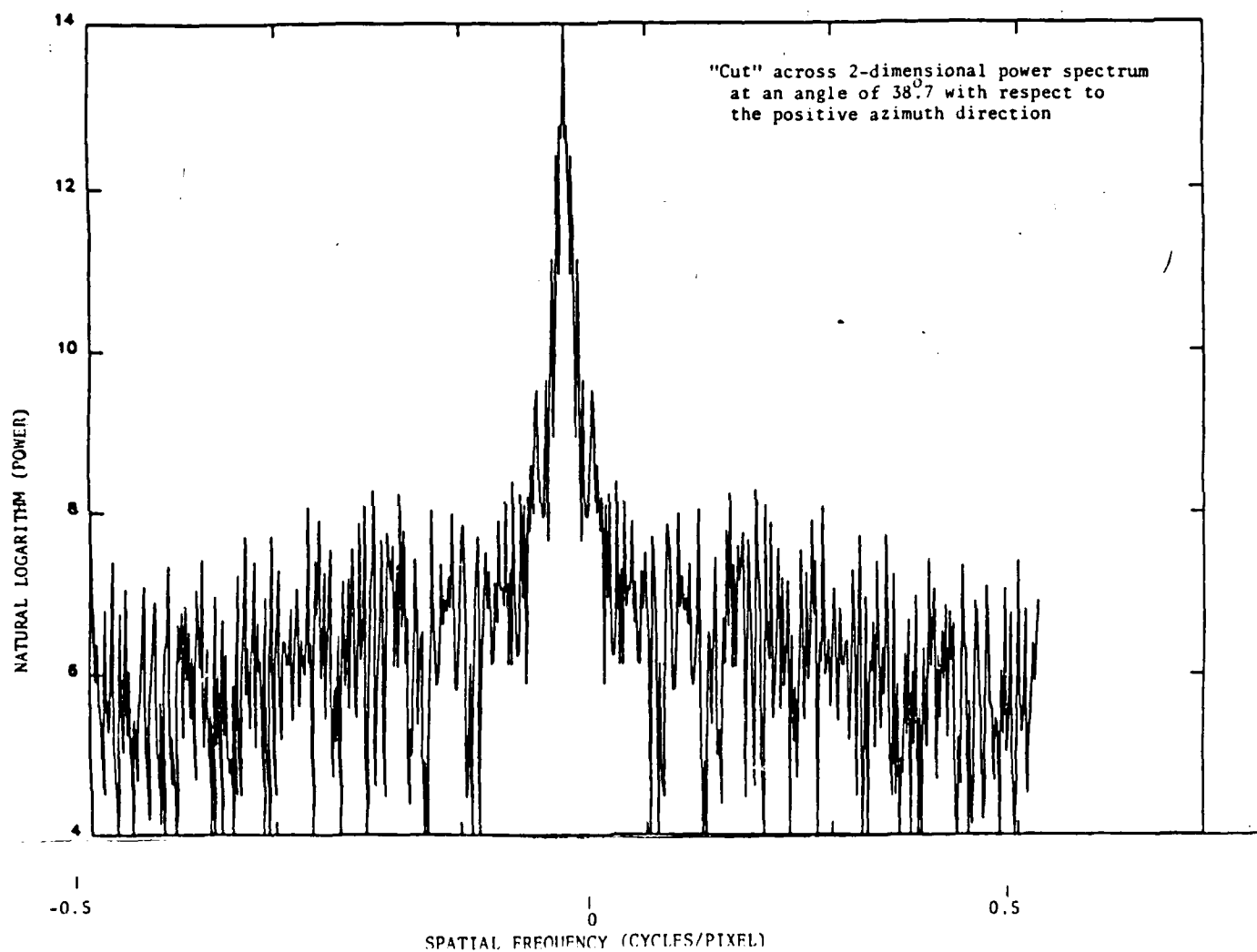


Figure 16

Full power spectrum of test area.

POWER SPECTRUM - REFERENCE AREA FOR COBB SEAMOUNT  
SEASAT SAR REV 466 IMAGE

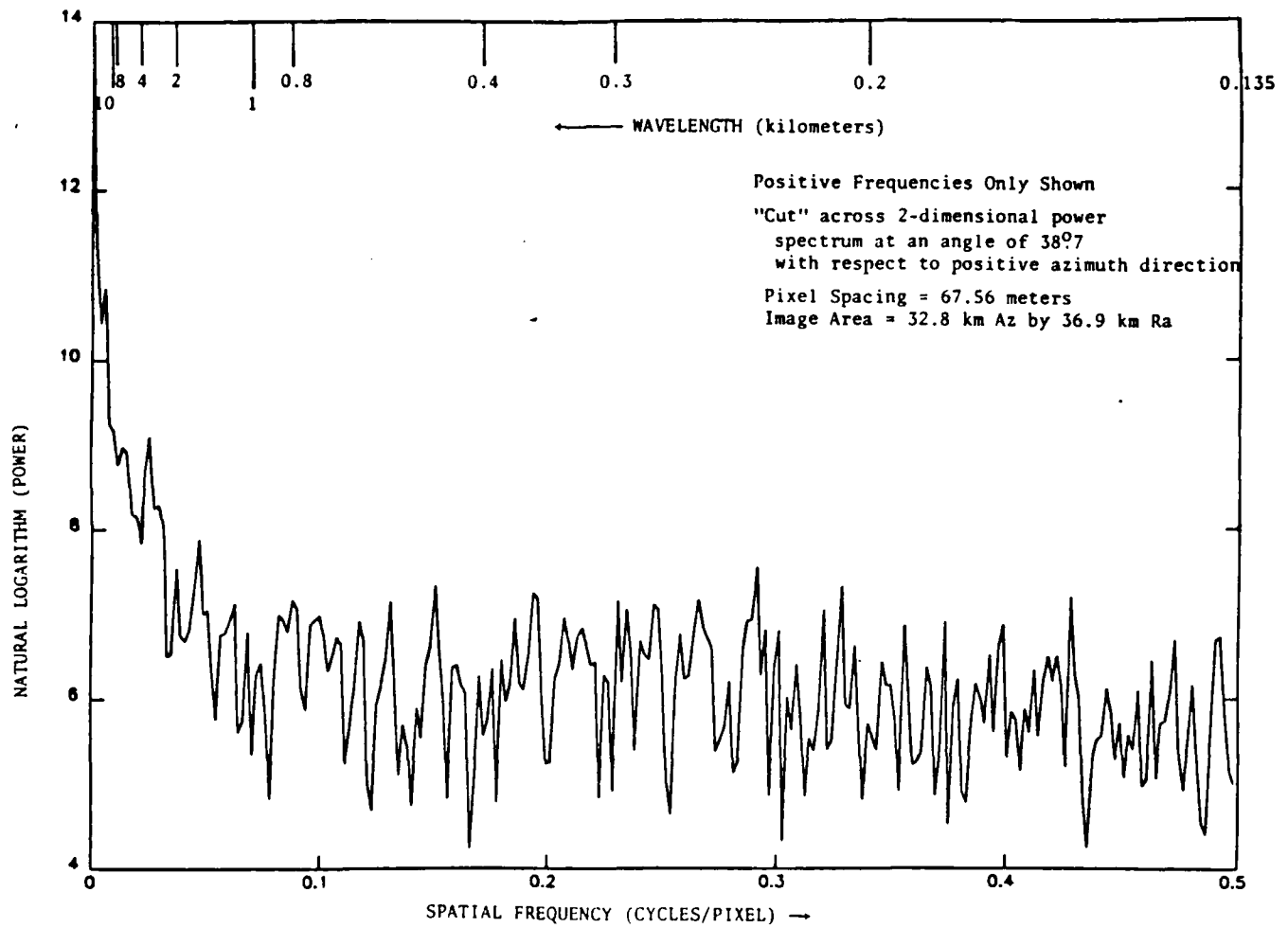


Figure 17

Half power spectrum of reference area.

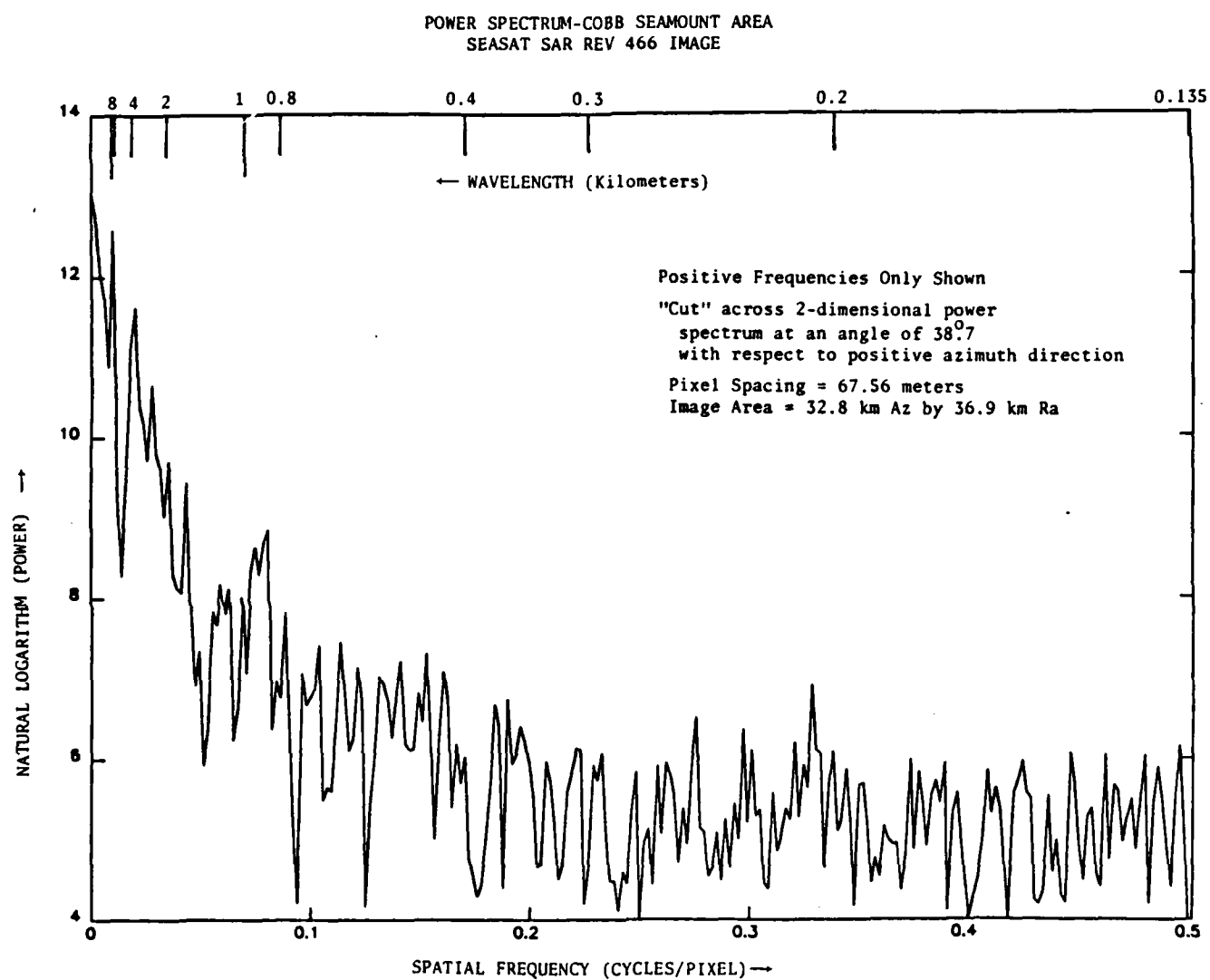


Figure 18

Half power spectrum of test area.

EXPANDED POWER SPECTRUM - COBB SEAMOUNT & REFERENCE AREA  
SEASAT SAR REV 466 IMAGE

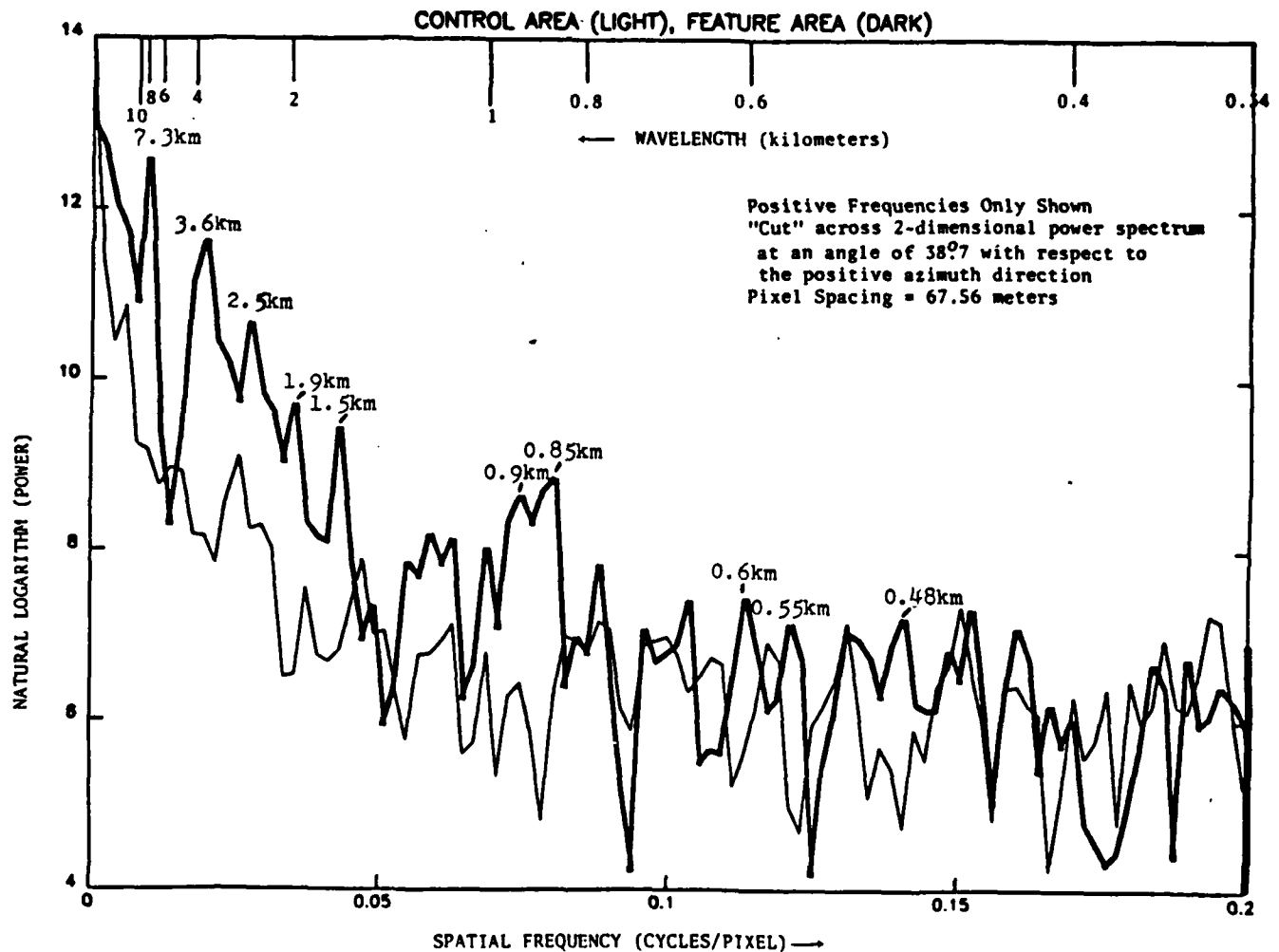


Figure 19

Comparison of half power spectrums of reference  
and test areas.

From the combined half power spectrums it can be shown that there is a significantly higher contribution to the power spectrum from longer wavelength waves in the target area as opposed to the reference area (Fig. 19). In particular, there are significant (relative gain of 9 dB or more) differences in the power associated with peaks at ten different wavelengths (Table 2). The standard cut off value for determining significance is a 6 dB gain over system noise (Mango, 1986). The system noise can not be determined from one image, but the noise level should be the same for both areas. The 9 dB relative gain level was selected to ensure that any changes in system noise between the two image areas would not effect the significance of peaks in the spectrum. There are also peaks, with less than 9 dB gain, at other long wavelengths, but these could be attributed to noise in original receipt of data, downlink transmission, and processing. There are no long wavelength significant peaks in the reference area spectrum.

All of the wavelengths, except the 0.48 km. wavelength, are enclosed in the predicted internal wave wavelength envelope. The 0.48 km. wavelength present outside the predicted envelope is most likely due to an error in the current estimate, placing the

<u>SIGNIFICANT WAVELENGTHS</u>			
<u>Wavelength (km.)</u>	<u>Power Target Area</u>	<u>Power Reference Area</u>	<u>Relative dB Gain</u>
7.26	12.52	9.16	14.6
3.61	11.59	8.16	14.9
2.51	10.70	8.40	10.0
1.91	9.70	6.50	13.9
1.58	9.35	6.78	11.2
0.89	8.70	6.40	10.0
0.85	8.81	6.00	12.2
0.60	7.40	5.20	9.6
0.55	7.10	4.90	9.1
0.48	7.15	4.80	10.2

Table 2  
Significant wavelengths.

cut off wavelength too long due to an over-estimation. The wavelengths are much too long for surface wind waves, which have wavelengths on the order of tens of meters or less. The peaks detected in the power spectrum must be from the surface manifestation of internal waves created by current flow over Cobb Seamount.

### CONCLUSIONS

Changes in the surface wave pattern are imaged by the SEASAT SAR sensor in the area of Cobb Seamount. The surface changes can be attributed to surface manifestations of hydrodynamic phenomena associated with current flow over seamounts. The particular phenomena imaged are bow waves and internal waves. Subtle manifestations of the bow waves are visible on the enhanced image indicating that they are present, but not highly developed in the Cobb Seamount area. The internal waves were predicted to be contained in an envelope of wavelengths greater than 0.5 km. Large wavelength surface patterns are visible in the imagery and are quantitatively measured using a power spectrum. Nine of the ten significant peaks found in the test area power spectrum are contained within the calculated envelope. The presence of a strong

thermocline and current in the region of Cobb Seamount support the conclusion that the peaks in the power spectrum are the surface manifestations of internal waves created by current flow over Cobb Seamount.



# APPENDIX A

Synthetic-aperture radar (SAR) is a high resolution imaging radar system which includes a sensor, data recording system, and a ground image processing computer system. The spacial resolutions achieved by SAR systems is on the order of tens of meters as opposed to the kilometer resolutions of standard radar sensors. The resolution, or ability to distinguish closely spaced objects in an image, is measured in two different directions: across the satellite ground track (range) and along the satellite track (azimuth).

The across track or range resolution, in the case of the SEASAT satellite SAR, is improved by the particular geometry used by the satellite system (Fig. A1). Standard radars image by transmitting an electro-magnetic pulse directly out and measuring the reflected energy. The SEASAT SAR instead uses a side-looking geometry. By looking to the side of the satellite ground track, the system develops a time difference between returns from the ground imaging swath regions closer to the satellite track (Fig.A2). The resolution is determined by:

$$\text{IFOVr} = \frac{1}{2} \frac{L_p * c}{\cos \theta} \quad \text{Eq.A1}$$

where IFOVr is the instantaneous field of view  
(resolution) in the range direction  
Lp is the pulse length in seconds  
c is the speed of light  
 $\theta$  is the grazing angle.

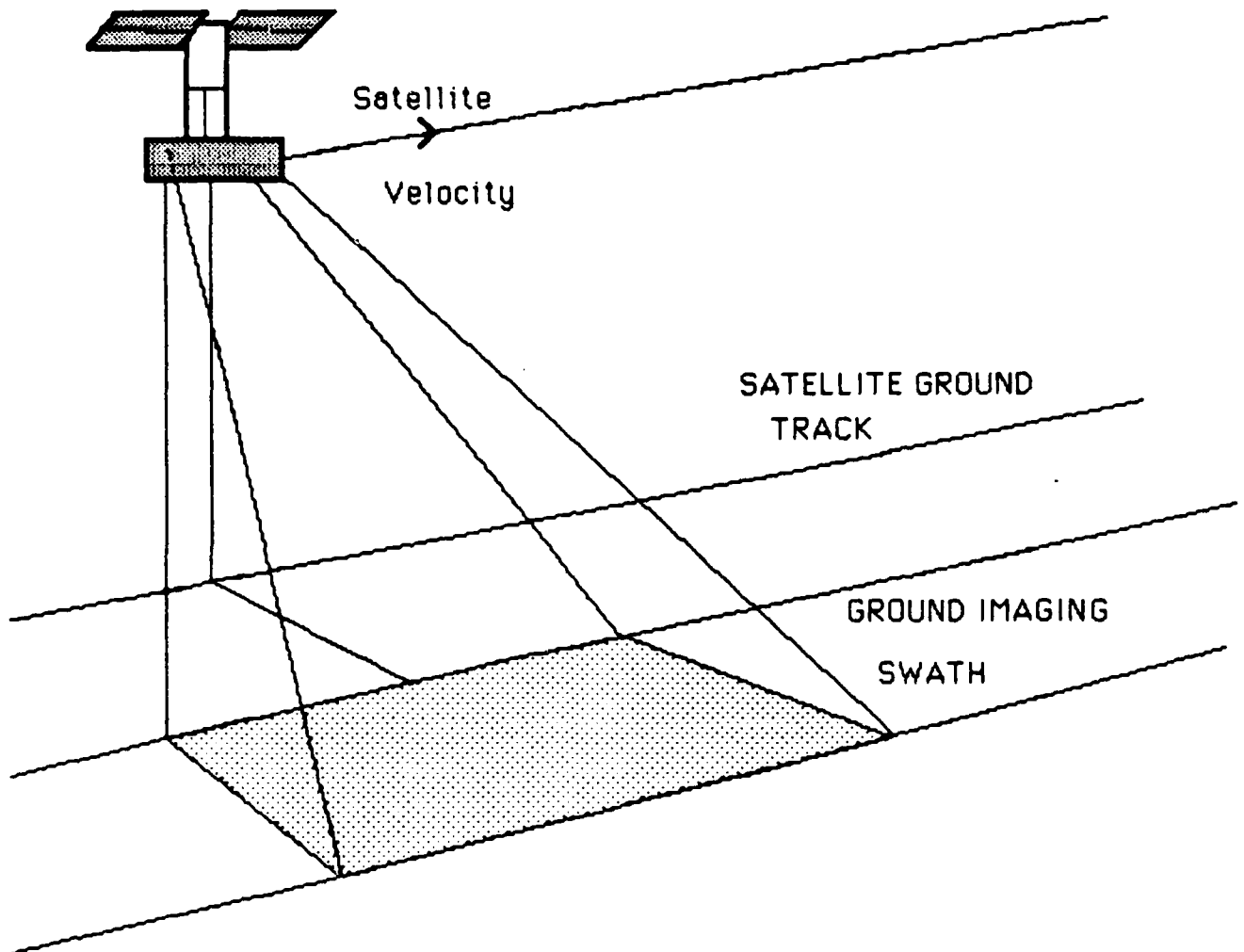


Figure A1  
SAR sensor geometry.

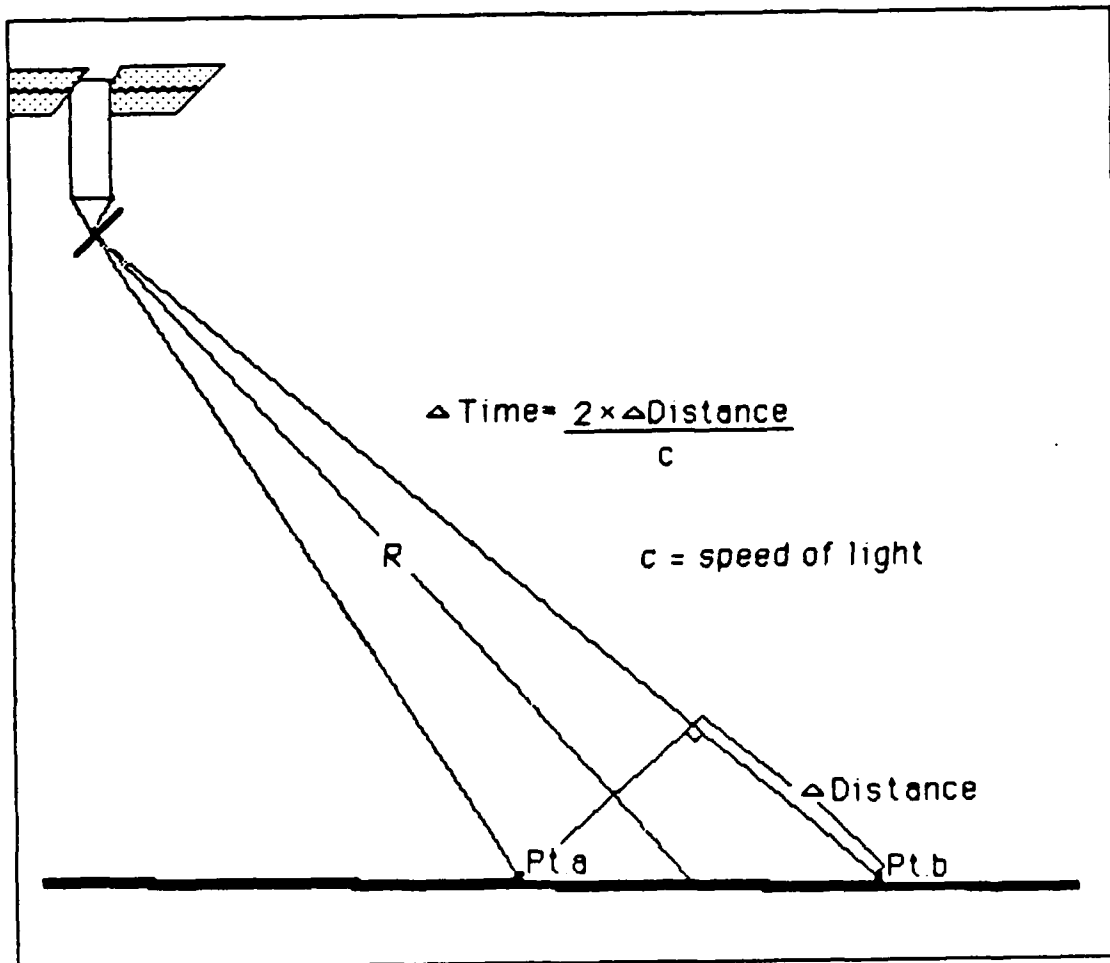


Figure A2

Developed time difference in return from  
ground points a and b.

The SEASAT SAR system has an across track resolution of approximately 21 meters.

Synthetic-aperture radar differs from traditional radars principally in the along track resolution. The equation governing radar resolution for the along track (azimuth) direction is:

$$\text{IFOVaz} = \frac{1}{2} \frac{\lambda * R}{D_{\text{az}}} \quad \text{Eq. A2}$$

where IFOVaz is the instantaneous field of view  
in the azimuth direction  
 $\lambda$  is the wavelength transmitted  
R is the slant range from the sensor to  
the ground imaging swath (Fig. A2)  
Daz is the antenna diameter in the  
azimuth direction.

For the SEASAT SAR sensor this would result in a resolution of 9 kilometers. The resolution is improved to the tens of meters desired by creating an antenna much larger than the 11m. by 2m. physical antenna carried by the SEASAT SAR sensor (Fig. A3). This antenna is an artificially created antenna or synthetic-aperture.

Synthetic-apertures are created by coherently adding multiple return pulses from an imaged area as the satellite travels through space. When the multiple pulses are coherently added together the processing system creates a single image. The image has a resolution equal to the resolution that would be possible using an antenna the size of the synthetic-aperture. The diameter of the synthetic-aperture is

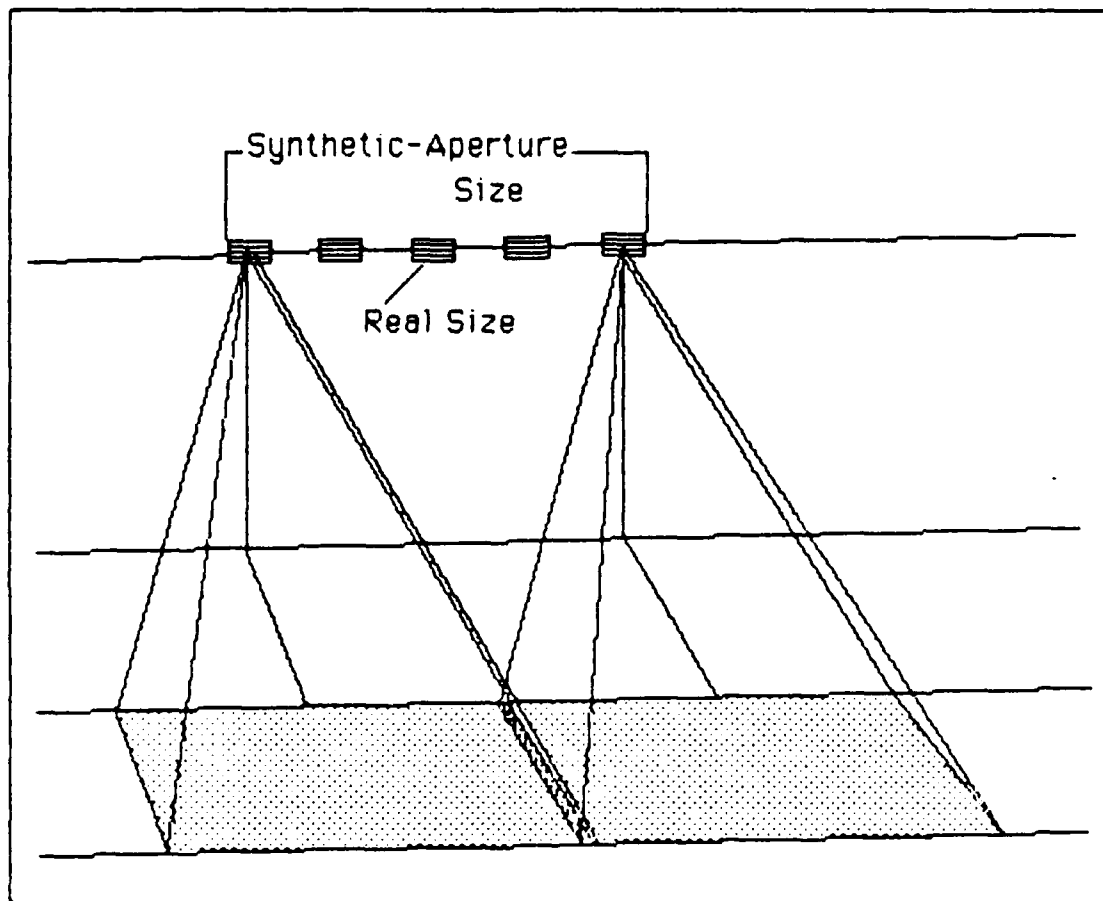


Figure A3

Real vs. Synthetic aperture size.

equal to the distance the satellite traveled while transmitting and receiving the multiple pulses. The developed synthetic-aperture length (Lsa) is:

$$Lsa = \frac{\lambda * R}{Daz} \quad \text{Eq. A3}$$

where Lsa is the synthetic-aperture length  
developed

$\lambda$  is the wavelength transmitted

R is the slant range

Daz is the diameter of the physical  
antenna.

The multiple pulse addition that creates the synthetic-aperture is known as coherent addition. Coherent addition is performed by the satellite retaining the Doppler history of a ground target's multiple returns as the ground target travels through the ground imaging swath. This Doppler history is then used to separate the signal return from a small area (on the order of 20 meters across).

The Doppler history is a recording of the multiple returns from a single area as both frequencies and intensities. As the satellite travels through space, a relative velocity is created between the satellite and the earth's surface area the satellite is imaging. This relative velocity creates a shift in the frequency returned by the area, to the satellite. This frequency shift is known as a Doppler shift. If the area to be imaged is ahead of the satellite the area will have a positive shift in

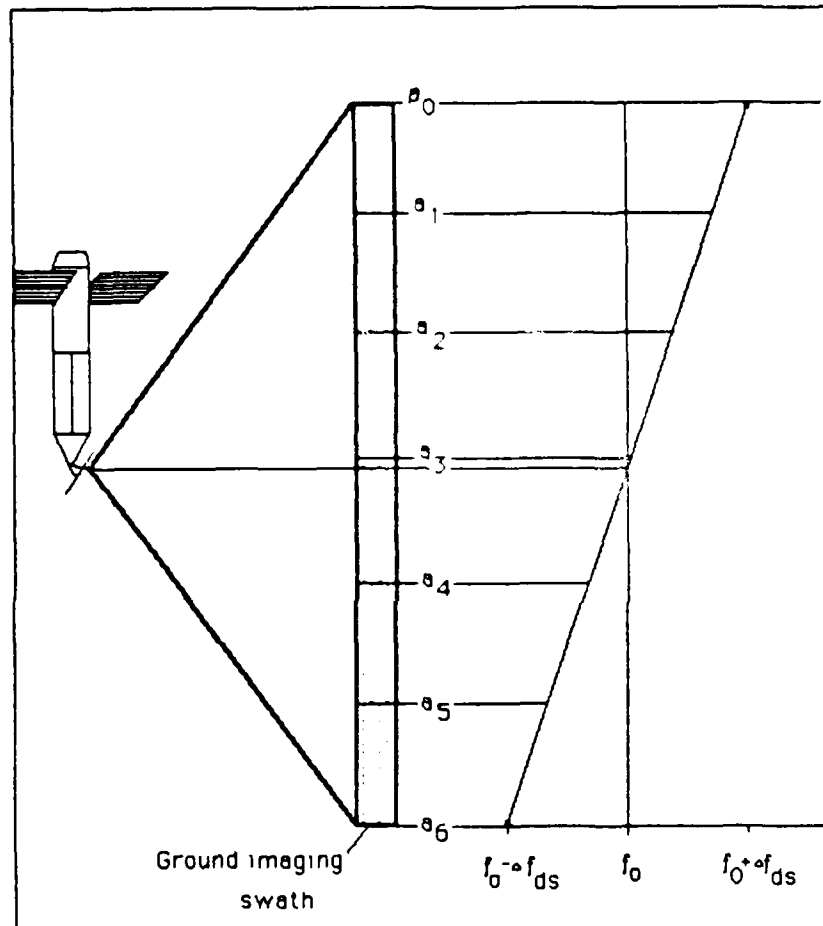
frequency as it enters the ground imaging swath. As the satellite continues through the imaging swath the Doppler shift will decrease until the area is perpendicular to the satellite track. When the area is perpendicular, the Doppler shift will be zero, and the return signal will have the same frequency as the original transmitted pulse. The Doppler shift will continue decreasing as the area goes through the imaging swath, with the shift being an increasingly negative value (Fig. A4).

The SAR system not only records the frequency Doppler history of each ground area, but also the return signal intensity associated with each return (Fig. A5). The coherent addition process takes the return signals, including both frequency and intensity, and adds the returns to determine the intensity of return when the Doppler shift equaled zero. This intensity is used as the intensity for the pixel area in the image produced.

The pixel size is determined by the resolution of the system. Taking the synthetic-aperture length (Eq. A3) as the antenna diameter and substituting that into Eq. A2 the resulting resolution is found:

$$\text{IFOVaz} = \frac{1}{2} \frac{\lambda * R}{L_{sa}} = \frac{D_{az}}{2} \quad \text{Eq. A4}$$

For SEASAT this allows a calculated resolution of 6 meters. Usually the processing system does not take



A point on the ground will first be imaged at point  $a_0$

The ground point will then be imaged at points  $a_1, a_2$ , etc.

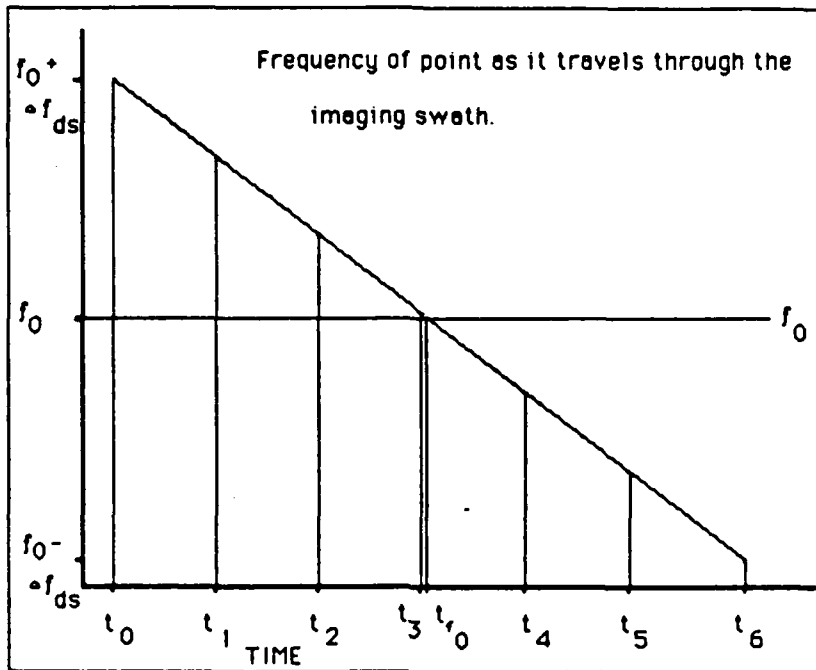
as the satellite continues on its velocity track.

Figure A4

Doppler shift of return signal (single return pulse).



## DOPPLER HISTORY OF ONE POINT - MULTIPLE LOOK (FREQUENCY)



## DOPPLER HISTORY OF ONE POINT - MULTIPLE LOOKS (INTENSITY)

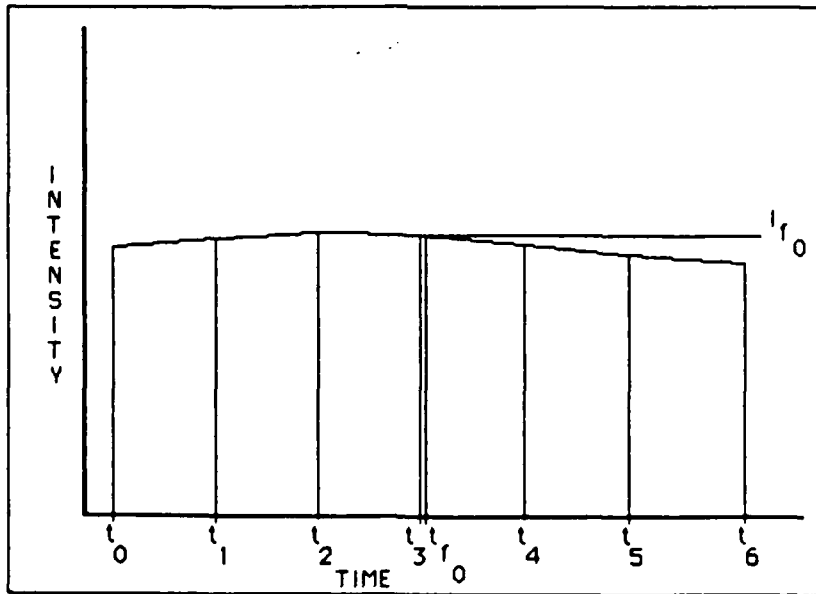


Figure A5

Doppler history of the multiple returns from one ground point (frequency and intensity).

full advantage of this achievable resolution. This is done to limit the image speckle effect intensified by full coherent addition. Instead only a part of the full synthetic-aperture is coherently processed. Coherent sub-apertures are then added together incoherently. This is called taking looks or multi-look processing. The result is that spacial resolution is compromised to reduce speckle. The images in this report were four look processed for an along track spacial resolution of about 24 meters.

### ACKNOWLEDGEMENTS

One of the hardest parts of doing research is that a scientist has to first face how little he knows. The challenge of research is to then find a way to fill in those areas that he doesn't understand. I have been most fortunate. While I started without a lot of knowledge about my research area, I was working in a research area with some of the most helpful and hard working people I have ever met. With their assistance I have been able to begin to understand the complexities of the sensor I have been working with and the ocean it is imaging. I would like to acknowledge these people without whom this report would not have occurred, because I would still be groping for answers if not for their assistance and encouragement.

In particular, I would like to thank: Benjamin Holt, John Curlander, and Jim Weirick of JPL; Steve Mango of NRL/DIPL; CDR Gott of the SEA USE Council; John Apel of APL; and LCDR Gleason, LCDR Welsh, and Lt Kinney of the Naval Academy Oceanography Department for their assistance in the collection, processing, and analysis of the huge amounts of data required for this project.

Additionally, I would like to thank the people

have provided the guidance necessary to prevent getting lost in the large array of data and options: Jerome Williams and Samuel McCandless.

Finally, I would also like to thank the person who has most contributed to the completion of this project, Paul Maughan, who reminded me that eventually all the fun had to end and a report had to be written, and then showed me how to write.

BIBLIOGRAPHY

- Alpers, W., and I. Hennings. "A Theory of the Imaging Mechanism of Underwater Bottom Topography by Real and Synthetic Aperture Radar". Journal of Geophysical Research. Vol. 89, No. 20. 1984.
- Apel, John. Personal interviews. 12 March and 24 April, 1986.
- Apel, John R., James R. Holbrook, Antony K. Liu, and John J. Tsai. "The Sulu Sea Internal Soliton Experiment". Journal of Physical Oceanography. Vol. 15. 1985.
- Beal, Robert C., Pat S. DeLeonibus, and Isadore Katz, Eds. Spaceborne Synthetic Aperture Radar for Oceanography. The Johns Hopkins University Press. Baltimore, London. 1981.
- Bell, T. H. Jr.. "Topographically Generated Internal Waves in the Open Ocean". Journal of Geophysical Research. Vol. 80, No. 3. 1975.
- Bell, T. H. Jr., A. B. Mays, and W. P. DeWitt. "Upper Ocean Stability - A Compilation of Density and Brunt-Vaisala Frequency Distributions for the Upper 500 m. of the World Ocean". NRL Report 7799 Naval Research Laboratory. Washington, D.C. 1974.
- Carver, Keith R., Charles Elachi, and Fawwaz T. Ulaby. "Microwave Remote Sensing from Space". Proceedings of the IEEE. Vol. 73, No. 6. 1985.

- Curlander, John C.. "Location of Spaceborne SAR Imagery". IEEE Transactions on Geoscience and Remote Sensing. Vol. GE-20, No. 3. 1982.
- Duntley, Seibert Q.. "Oceanography from Manned Satellites by Means of Visible Light". Oceanography from Space. Woods Hole Oceanographic Institute. Woods Hole, MA.. 1965.
- Ewing, Gifford C.. Ed.. Oceanography from Space. Woods Hole Oceanographic Institution. Woods Hole, MA.. 1965.
- Fu, Lee-Lueng, and Benjamin Holt. "Internal Waves in the Gulf of California: Observations from a Spaceborne Radar". Journal of Geophysical Research. Vol. 89, No. C2. 1984.
- Fu, Lee-Lueng, and Benjamin Holt. SEASAT Views Oceans and Sea Ice With Synthetic-Aperture Radar. JPL Publication 81-120. 1982.
- Garrett, Christopher, and Walter Munk. "Internal Waves in the Ocean". Annual Review of Fluid Mechanics. 1979.
- Gordon, C., D. Greenwalt, and J. Witting. "Surface-Wave Expression of Bathymetry Over a Sand Ridge". Remote Sensing of Shelf Sea Hydrodynamics. Elsevier Science Publishers. B.V. Amsterdam. 1984.
- Harger, Robert O.. Synthetic-Aperture Radar Systems. Academic Press. New York, New York. 1970.

- Hovanessian, S. A.. Radar System Design and Analysis.  
Artech House, Inc. Dedham, MA. 1984.
- Johns Hopkins APL. Johns Hopkins APL Technical  
Digest. Vol. 6, No.4. 1985.
- Kasischke, Eric S., Robert A. Shuchman, and David R.  
Lyzenga. "Detection of Bottom Features on SEASAT  
Synthetic Aperture Radar Imagery". Photogrammetric  
Engineering and Remote Sensing. Vol. 49, No. 9.  
1983.
- Kasischke, Eric S., Guy A. Meadows, and Philip L.  
Jackson. The Use of Synthetic Aperture Radar  
Imagery to Detect Hazards to Navigation.  
Defense Mapping Agency. Washington, D.C. 1984.
- Kasischke, Eric S., Y. C. Tseng, G. A. Meadows, and  
A. K. Liu. "Observations of Internal Waves and  
Frontal Boundaries on SEASAT SAR Imagery Collected  
Over the Eastern North Atlantic Ocean". Presented  
at the Seventeenth International Symposium on  
Remote Sensing of the Environment, Ann Arbor, MI.  
1983.
- Kinsman, Blair. Wind Waves: Their Generation and  
Propagation on the Ocean Surface. Dover  
Publications, Inc. New York, NY. 1984.

Liu, Antony K., James R. Holbrook, and John R. Apel.

"Nonlinear Internal Wave Evolution in the Sulu Sea". Journal of Physical Oceanography. Vol. 15, No. 12. 1985.

Mango, Steven. Personal interviews. Nov. 1985 to Apr. 1986.

Maskell, S. J.. Eddy Generation by Seamounts. Oxford Computer Services Limited. Portland, England. 1984.

Maughan, Paul McAlpine. Observations and Analysis of Ocean Currents Above 250 Meters Off the Oregon Coast. Masters Thesis Report. Oregon State University. 1963.

Maxworthy, T.. "A Note on the Internal Solitary Waves Produced by Tidal Flow Over a Three-Dimensional Ridge". Journal of Geophysical Research. Vol. 84, No. C1. 1979.

Maxworthy, T.. "On the Formation of Nonlinear Internal Waves From the Gravitational Collapse of Mixed Regions in Two and Three Dimensions". Journal of Fluid Mechanics. Vol. 96, Part 1. 1980.

McCandless, Samuel Walter, and Charmaine P. Mrazek. Analysis of Oceanic Subsurface Features Using Space Based Radar Imagery. Underwater Systems, Inc.. Rockville, MD. 1982.



- Meadows, G. A., R. A. Shuchman, Y. C. Tseng, and  
E. S. Kasischke. "SEASAT Synthetic Aperture Radar  
Observations of Wave-Current and Wave-Topographic  
Interactions". Journal of Geophysical Research.  
Vol. 88, No. C5. 1983.
- Phillips, O. M.. The Dynamics of the Open Ocean.  
Second Edition. Cambridge University Press.  
Cambridge, England. 1977.
- Pond, Stephen, and George L. Pickard. Introductory  
Dynamical Oceanography. Second Edition. Pergamon  
Press. Oxford, England. 1983.
- Pravdo, Steven H., Bryan Huneycutt, Benjamin M. Holt,  
and Daniel N. Held. SEASAT Synthetic-Aperture  
Radar User's Manual. JPL Publication 82-90. 1983.
- Robinson, I. R.. Satellite Oceanography: an  
Introduction for Oceanographers and Remote-Sensing  
Scientists. Ellis Horwood Limited. Chichester,  
England. 1985.
- Schwinderski, E. W.. Global Ocean Tides, Part III.  
Various constituents. Naval Surface Weapons  
Center. NSWC TR 81-122. 1981.
- Shuchman, Robert A., Andrew L. Maffett, and Alex  
Klooster, Jr.. "Static and Dynamic Modeling of a  
SAR Imaged Ocean Scene". IEEE Journal of Oceanic  
Engineering. Vol. OE-6, No. 2. 1981.

Shuchman, R. A., A. Klooster, and A. L. Maffett.

"Synthetic Aperture Radar Modeling of Surface  
Ocean Waves". ONR Contract N00014-76-C-1048.

Vesecky, John F., Martha P. Smith, David A.

Napolitano, and Stephen L. Durden. "Models for the  
Imaging of Ocean Gravity Waves by SAR --  
Comparisons of Theory and Experiment". Conference  
Record. Oceans 84. 1984.

END

DTIC

10-86